Geomechanical modelling of sinkhole development using Distinct Elements: Model verification for a single void space and application to the Dead Sea area

Djamil Al-Halbouni[1], Eoghan P. Holohan[2], Abbas Taheri[3], Martin P. J. Schöpfer[4], Sacha Emam[5] and Torsten Dahm[1,6]

[1]Helmholtz Centre - German Research Centre for Geosciences (GFZ), Section 2.1, Telegrafenberg, Potsdam 14473, Germany.
[2]UCD School of Earth Sciences, University College Dublin, Belfield, Dublin 4, Ireland.
[3]School of Civil, Environmental and Mining Engineering, University of Adelaide, Adelaide, South Australia 5005, Australia.
[4]Department for Geodynamics and Sedimentology, University of Vienna, Athanstrasse 14, A-1090, Vienna, Austria
[5]Geomechanics and Software Engineer, Itasca Consultants S.A.S, Écully, France
[6]Institute of Earth and Environment, University of Potsdam

Correspondence to: Djamil Al-Halbouni (halbouni@gfz-potsdam.de)

Abstract. Mechanical and/or chemical removal of material from the subsurface may generate large sub-surface cavities, the destabilisation of which can lead to ground collapse and the formation of sinkholes. Numerical simulation of the interaction of cavity growth, host material deformation and overburden collapse is desirable to better understand the sinkhole hazard, but is a challenging task due to the involved high strains and material discontinuities. Here we present 2D Distinct Element Method numerical simulations of cavity growth and sinkhole development. Firstly, we simulate cavity formation by quasi-static, step-wise removal of material in a single growing zone of an arbitrary geometry and depth. We benchmark this approach against analytical and Boundary Element Method models of a deep void space in a linear elastic material. Secondly, we explore the effects of properties of different uniform materials on cavity stability and sinkhole development. We perform simulated biaxial tests to calibrate macroscopic geotechnical parameters of three model materials representative of those in which sinkholes develop at the Dead Sea shoreline: mud, alluvium and salt. We show that weak materials do not support large cavities, leading to gradual sagging or suffusion style subsidence. Strong materials support quasi-stable to stable cavities, the overburdens of which may fail suddenly in a caprock or bedrock collapse style. Thirdly, we examine the consequences of layered arrangements of weak and strong materials. We find that these are more susceptible to sinkhole collapse than uniform materials not only due to a lower integrated strength of the overburden, but also due to an inhibition of stabilising stress arching. Finally, we compare our model sinkhole geometries to observations at the Ghor Al-Haditha sinkhole site in Jordan. Sinkhole depth to diameter ratios of 0.15 in mud, 0.37 in alluvium and 0.33 in salt are reproduced successfully in the calibrated model materials. The model results suggest that the observed distribution of sinkhole depth/diameter values in each material type may partly reflect sinkhole growth trends.

1   Introduction

Sinkholes are enclosed surface depressions in sediments and rocks. They commonly result from subsidence of overburden into void space that is generated through the physical-chemical removal of material in the underground. In the final stage of a sinkhole process, a sudden collapse of the overburden may occur (Gutiérrez et al., 2014; Waltham et al., 2005). Removal of material and void formation in the underground is usually related to hydraulic flow and to associated dissolution or physical erosion of material, or both. Subsidence may occur continuously over a long time depending on the flow conditions and material properties (Goldscheider and Drew, 2007; Parise and Gunn, 2007; Waltham et al., 2005). Depending on the properties of the overburden (cover or caprock) and the evolution stages, different sinkhole morphologies can be described. Typical endmembers can be defined (Figure 1, see *Gutiérrez et al.,* 2008, 2014).
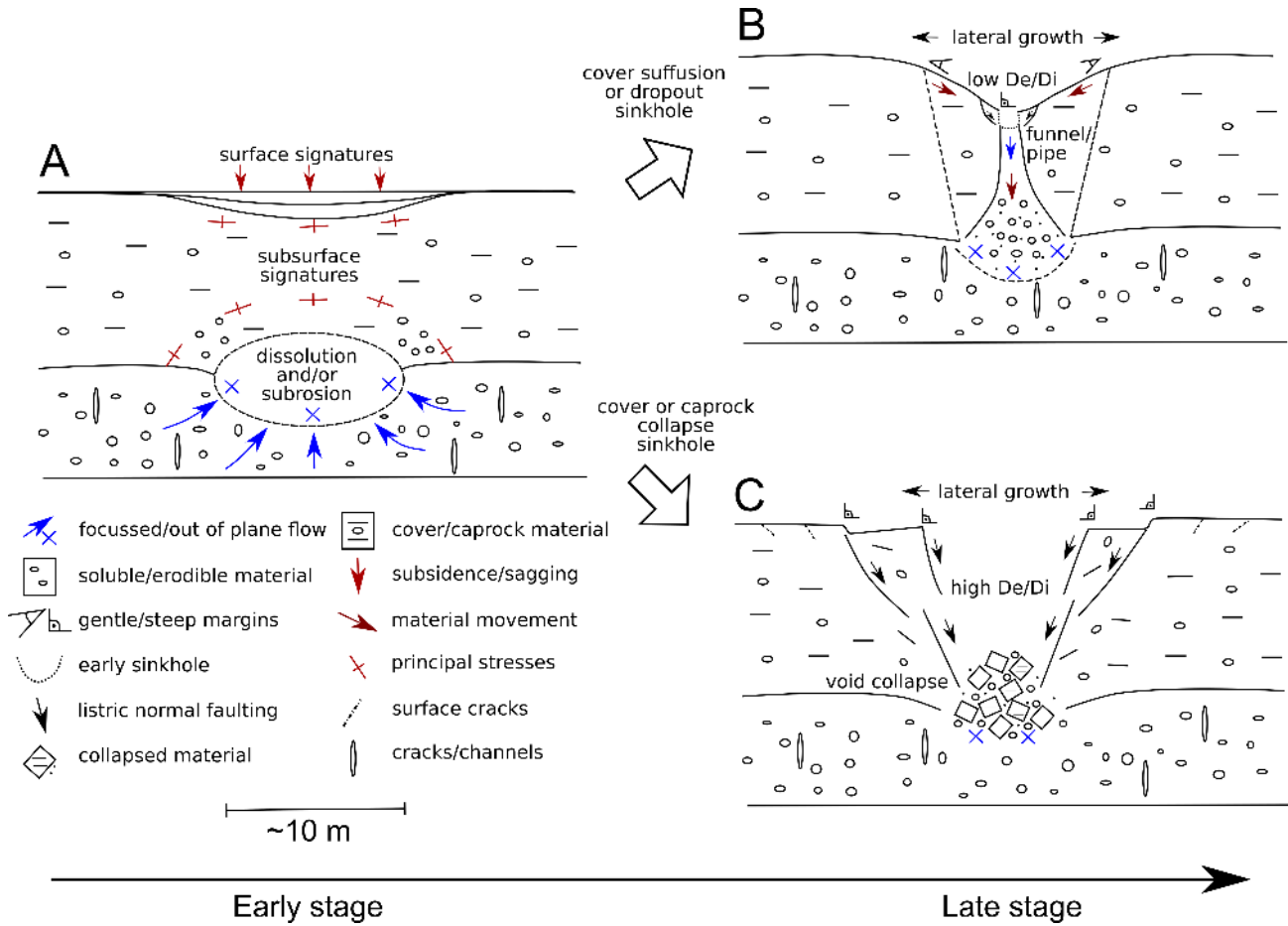
Figure 1: Conceptual models of sinkhole formation. (A) Sub-surface dissolution or/and subrosion caused by focussed flow in soluble/weak material. (B) Cover suffusion or dropout sinkhole that forms by material transport through a pipe or along a funnel. A weak cover material slumps into the voids and creates a sinkhole with low depth/diameter ratio and flat to steep margins depending on the material cohesion. (C) Cover or caprock collapse sinkhole. Large voids may stay initially stable in a strong material, but their growth leads to a sudden overburden collapse. The formed sinkholes have usually a high depth/diameter (De/Di) ratio and contain steep margins with large ground cracks. Both sinkhole types represent late stage endmembers and mixtures of both are very common in nature (Figure 2).

1.1 Sinkhole development at the Dead Sea

The Dead Sea is a hypersaline terminal lake and is one of the world's most active areas of sinkhole development. More than 6000 sinkholes have formed there at an increasing rate over the last 35 years (Abelson et al., 2017). Previous studies relate the sinkhole formation at the Dead Sea to the regression of the lake, which is ongoing since the 1960s, and to the consequent invasion of evaporite-rich sedimentary deposits around the Dead Sea by relatively fresh groundwater. Evaporitic minerals in the sediments are susceptible to dissolution, while the non-evaporitic sedimentary materials are weak (poorly-consolidated or unconsolidated) and can easily be physically eroded by subsurface flow ('piping'). Some studies have highlighted the role of subrosion, i.e. both mechanical and chemical (leaching) erosion of the subsurface (Wadas et al., 2016), in the development of sinkholes (Al-Halbouni et al., 2017; Arkin and Gilat, 2000; Polom et al., 2018), while others have focussed on the role of dissolution only in generating large cavity development in a relatively shallow but thick salt layer (Ezersky and Frumkin, 2013; Taqieddin et al., 2000; Yechieli et al., 2006).

In this paper, we draw upon observations from the sinkhole site of Ghor Al-Haditha (N31° 18' 45", E35° 31' 52") on the southeaster shore of the Dead Sea in Jordan (Figure 2 Figure 3). Sinkhole development in the area is active since 1986 (Sawarieh et al., 2000), with ongoing damage or destruction of infrastructure and agriculture. As of 2018, the cumulative number of sinkholes formed there has passed one thousand (Watson et al., 2018). Photogrammetric datasets have been acquired in 2014, 2015 and 2016 to produce high-resolution and high-accuracy Digital Surface Models and Orthophotos for the Ghor Al-Haditha sinkhole site. Although the results for 2015 and 2016 shown below in this paper are new, the methodology of their generation is the same as for the 2014 survey, which is described in detail by *Al-Halbouni et al.,* 2017.

Figure 2: Sinkhole examples from the eastern shoreline of the Dead Sea. (A) Sinkhole with De/Di ~ 0.15 formed in semi-consolidated lime-carbonate mud of the former Dead Sea bed. (B) Sinkhole with De/Di ~ 0.33, formed in semi-consolidated sandy-gravel (alluvial) sediment. Note the deep cracks and tilted blocks marginal to the sinkhole. (C) Sinkhole with De/Di ~ 0.33 formed in semi- to well-consolidated salt material. Note the typical overhanging sides and pronounced cracks in the surroundings.

Sinkholes form in the three 'end-member' near-surface materials at the Ghor Al-Haditha sinkhole site (Figure 2): (1) unconsolidated to semi-consolidated lacustrine clayey carbonates ('mud') with interleaved thin evaporite layers; (2) unconsolidated to semi-consolidated alluvial sand-gravel sediments; (3) rock salt (mainly halite) with interleaved thin mud

layers. The main morphological distinction is that narrower and deeper sinkholes occur in the 'alluvium' and in the 'salt' (Figure 3B, C), whereas wider and shallower sinkholes occur in the 'mud' (Figure 3A). Many sinkholes in the alluvium and especially in the salt have overhanging sides and/or large marginal blocks and deep (up to several meters) concentric ground cracks. The alluvium and the salt can sustain meter-scale or multi-meters cavities associated with sinkhole development (Al-Halbouni et al., 2017; Closson and Abou Karaki, 2009; Yechieli et al., 2006). The mud sinkholes commonly contain a wide peripheral zone of back rotated blocks delimited by small faults that down-throw towards the centre. Ground cracks are commonly also well developed around sinkholes in the mud, but are not as deep (up to a few 10's of cm) as in the other materials.
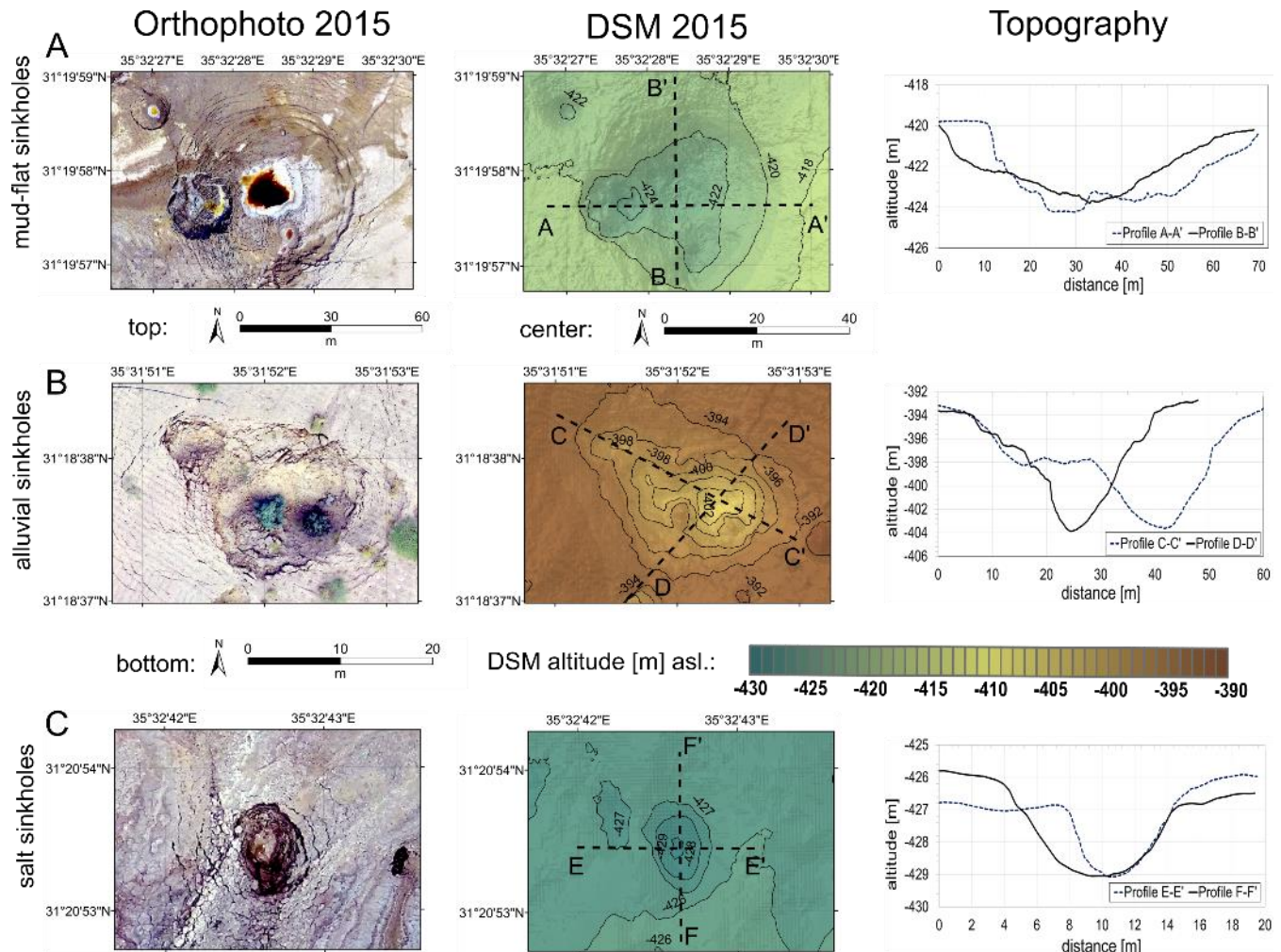
Figure 3: Representative morphological data from single sinkholes at the eastern shoreline of the Dead Sea. (A) In the mud-flat, (B) in the alluvial material and (C) in the salt cover. Shown here are orthophotos (left column), Digital Surface Models (DSM, middle column) and topographic cross-sections (right column) with a resolution of 10 cm and an accuracy of 12/17 cm (H, V). These were

created from low altitude aerial images acquired in 2015 and processed by Structure-from-Motion photogrammetry. Contours of elevation in meters are indicated for clarity on the DSM, which is plotted in the same colour scale for all materials.

1.2 Numerical modelling of sinkhole development

The numerical simulation of sinkhole development is of interest to understand better the processes of sinkhole formation and
5 the related hazard. Continuum-mechanics approaches ((Carranza-Torres et al., 2016; Fazio et al., 2017; Fuenkajorn and Archeeploha, 2010; Parise and Lollino, 2011; Rawal et al., 2016; Salmi et al., 2017)) have generally defined a single cavity in an elastic or elasto-plastic half-space and assessed the static threshold strength of the overburden to predict mechanical failure. This approach is possibly suitable for assessing the factor of safety of an individual, fully-developed cave and for deriving a relation between measured surface subsidence and cavern configuration. However, the geometries of voids involved in
10 sinkhole development are often non-singular, irregular and distributed on lots of scales (Abelson et al., 2017; Al-Halbouni et al., 2017; Ezersky et al., 2017; Gutiérrez et al., 2016; Parise et al., 2018; Yizhaq et al., 2017). Alternatively, continuum-based corrosion models have addressed the rock dissolution and void growth in a hydrogeological framework ((Kaufmann and Romanov, 2016; Shalev and Lyakhovsky, 2012)). This approach has the advantage of accounting for geometrically-complex or stochastic void development and the role(s) of material heterogeneity, but it does not account for effects of overburden
15 instability. Both of these past continuum-based approaches have neglected the mechanical consequences of void growth and the explicit simulation of sinkhole collapse.

Distinct Element Method (DEM) modelling is increasingly used in geoscience for numerical simulation of large-strain and discontinuous rock deformation (Cundall and Strack, 1979; Potyondy and Cundall, 2004). The main advantage of the DEM is
20 its ability to simulate rock samples or rock masses as an assemblage of discrete particles or blocks, which can undergo large displacements and rotations. The method uses a so-called Soft Contact approach where the particles are rigid, but allowed to overlap at contact points. Based on updated particle positions, the contacts between particles are automatically detected or deleted during the simulation. Based on the relative displacement and velocity of the particles in contact, interaction laws are used to update the forces and moments transmitted through the contacts. The resultant forces and moments accumulated on
25 each particle are subsequently used to solve Newton's second law of motion and to update the particle's position and velocity. Elasto-plastic bonds of finite strength can be accounted for in the interaction law, and enable a quasi-continuum behaviour at assembly scale; which can evolve to highly discontinuous deformation as bonds between particles break and damage develops. In this way, the DEM can overcome limitations of continuum-based numerical simulation of large and highly localised strains in discontinuous media (Jing and Stephansson, 2007). Using the DEM, recent advances have been made in, for example, rock
30 mechanics (Schöpfer et al., 2009), slope stability and mass movements (Thompson et al., 2010), mine or tunnel stability (Bonilla-Sierra et al., 2012), synthetic rock mass modelling (Ivars et al., 2011), fracture growth (Schöpfer et al., 2016), hydrofracture and caldera subsidence analysis (Holohan et al., 2011, 2015, 2017).

For modelling sinkhole collapse, *Baryakh et al.,* [2008, 2009] used the DEM to conduct simple stability tests and mechanical analyses for a single, instantaneously-generated cavity of varying geometry, depth and overburden mechanical properties. Other studies have adopted a similar approach but also included Discrete Fracture Networks (DFNs) that represent pre-defined or empirically determined discontinuities (joints, faults) within rock masses (Hatzor et al., 2010). DEM coupled with Finite

5   Element Modeling (FEM) has been used for simulating mechanical failure above a large salt cavity (Mercerat, 2007), but the DEM part was limited to a single rock layer within the overburden. Again, the main shortcoming of these earlier DEM-based studies is that cavity growth and related mechanical development were not explicitly simulated.

1.3   Contribution of this paper

This paper reports the first two-dimensional DEM simulations of sinkhole formation that explicitly simulate both void growth

10   and overburden collapse. In part, the approach of void growth adopted here is similar to that in a recent work on mine caving (Sainsbury, 2012). Our study builds upon the previous works of *Caudron et al.*, [2006] and *Baryakh et al.*, [2008, 2009], but goes further in calibration of geomechanical behaviour, in complexity of process and in application to natural sinkholes. As in many previous studies, we focus here on the creation, growth and instability of a single void leading to a single sinkhole. We use the general-purpose commercial DEM software Particle Flow Code (PFC), developed by Itasca Consulting Group Inc.

15   (Potyondy, 2014b). Further details of the DEM, as implemented in PFC2D, are covered in Appendix A. Note that in accordance with PFC2D convention, compressive stress is taken as negative throughout this manuscript.

Regarding the structure of this paper, we begin by summarising tests on model resolution, model dimensions and void creation procedures, and we show results of benchmarking to continuum-based solutions for displacement around a void. We then show

20   the results of calibration tests that were used to tune the bulk geomechanical behaviours of the DEM particle assemblies. Following this, we analyse the evolution stages of model void growth and sinkhole collapse for uniform and layered materials. We then compare the morphological parameters at the Ghor Al-Haditha survey site to those predicted by our models. In the final part, an outlook to future improvements and applications is given.

2   A Distinct Element Method approach for modelling cavity and sinkhole formation

25   In this section, we report on convergence and benchmarking tests for the DEM model as pertained to cavity generation. To this end, we firstly simulate a material that behaves elastically by using bond strength and cohesion values at the upper limit of realistic rock strengths (cf. Table 1). We also report on the material parameter calibration by simulated biaxial compression and tension tests applied to the numerical materials mimicking those common at the Dead Sea region. Finally, we summarise the final procedure for cavity growth that is based on these tests, but implemented under conditions in which the DEM model

30   material is weak enough to fail and to lead to sinkhole formation.
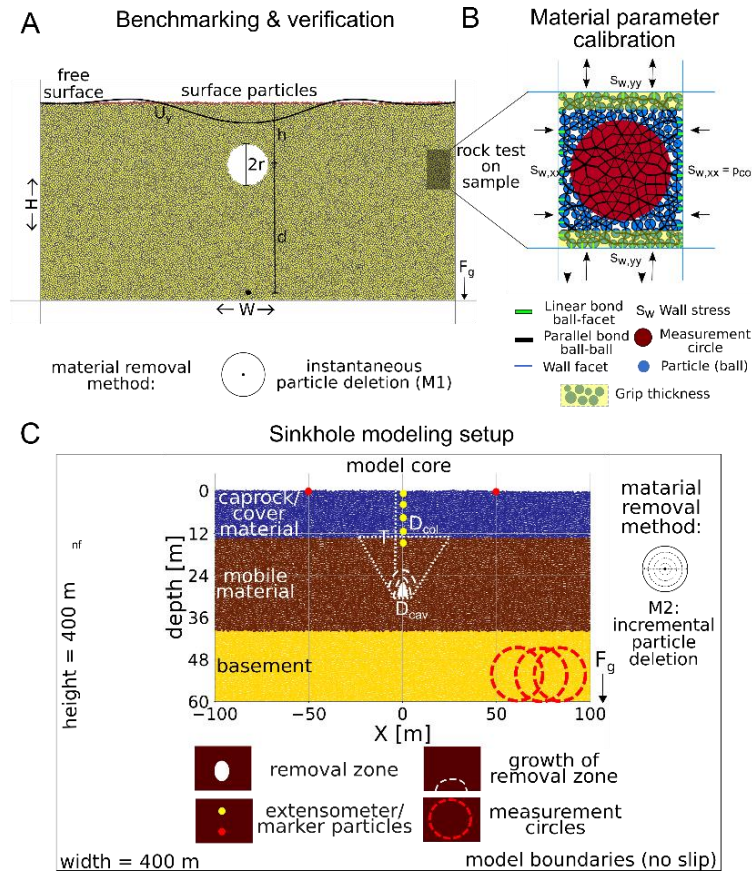
Figure 4: Setups for model benchmarking, calibration and sinkhole simulation. (A) model verification and benchmarking. A circular cavity of radius r = 5 m is placed instantaneously at a depth h = 35 m and a distance d=H-h from a fixed point at the bottom of a box of varying dimensions H × W and particles of radii R subject to the body force due gravitational acceleration F_g. **(B)** rock tests for material parameter calibration. A sample is contained within walls that are used for applying confining pressure simulating the materials' response at different depth. A servo-mechanism controls the walls' axial velocity. For a tensile test, grips of certain thickness are defined at the bottom and top of the sample and moved outwards. **(C)** sinkhole simulation by quasi-static incremental single void growth. T/D is referring to the overburden thickness to diameter ratio of either a stable cavity (D = D_{cav}) or an unstable collapse zone (D = D_{col}). Yellow/red circles represent particles that act as extensometers/markers respectively. Big red circles indicate overlapping measurement circles distributed within an area of interest.

2.1   Determination of the optimal void space installation and model dimensions

We tested model sensitivity to resolution, dimension and void installation method. In a first test, different void space installation methods were compared in terms of computation time. For this, surface particle displacement was tracked above a cavity of 5 m radius placed at 35 m depth (Figure 4A), an assumed realistic subrosion zone depth and dimension. Two methods utilized a particle deletion scheme, while two other methods were based on particle radii reduction. No substantial differences in the vertical and horizontal surface displacements were observable, i.e. the methods did not affect the outcome of the elastic solution, but the particle deletion scheme was one order of magnitude faster than radii reduction. Hence the particle deletion

scheme was chosen as appropriate for the following tests and the sinkhole models. More details on the results and the set of investigated parameters can be found in Appendix B.1.

In a second test, model width, height and particle radii were varied to determine the optimal model dimensions for the problem of a void space in the subsurface. The void installation method based on instantaneous particle deletion was applied. The final results indicates that symmetric boundaries of H × W = 400 × 400 m with a particle mean radius of 0.32 m yields the best results. These model dimensions and resolution were hence chosen for the main model set reported below. Details on the convergence tests that led to this choice of dimensions and resolution can be found in Appendix B.2.

2.2   Benchmarking of the DEM approach against analytical solutions and BEM

We performed a benchmarking of surface displacements in the DEM cavity development models with displacements derived from different continuum-based approaches. Cavity depth and size, model dimensions (Figure 4A) and the bulk elastic parameters of the DEM material in Table 1 serve as input parameters for two analytical solutions and for a boundary element (BEM) numerical model.

Table 1: Bulk properties of the particle assemblies used in the benchmarking of DEM cavity formation models versus analytical solutions and BEM.

Bulk Parameter [unit]	Symbol	Unit	Value
Porosity[1]	n	-	0.16
Density[1]	ρ_{bulk}	[kg/m^3]	2100
Earth pressure coefficient at rest[1]	K_0	-	0.26
Young's modulus[2]	E	[GPa]	5.337 ± 7^{-3}
Poisson-ratio[2]	ν	-	0.39 ± 0.03

The analytical solutions are for a circular cavity in a gravity loaded, infinite, linear elastic full/half space under plane strain conditions (Kirsch, 1898; Verruijt and Booker, 2009). The Kirsch solution is a classical full-space solution for simple excavation shapes, but does not include the free-surface effect; mathematical details are provided by *Brady and Brown*, [2006]. The *Mindlin*, [1940] solution is for stresses around tunnels and includes free-surface effects; mathematical details are given by *Verruijt and Booker,* [2009]. The input values for the Mindlin analytical solution are $d/h = 4$, $E = 5\ GPa$, $\nu = 0.39$ and $K_0 = 0.26$. The reader is referred to Appendix B.3 for more details on the effect of *d* and *E*.

---

[1] Estimation based on measurement circles in five different particle assemblies at a depth of 35 m.
[2] Estimation based on fitting of measurement circle data in ten different simulated rock tests. Compare Section 2.4.

The Boundary Element Method (BEM) model is based on a code by *Nikkhoo and Walter* [2015] and simulates the surface displacements along a cross-section above a 3D cylindrical void space. The void space is simulated as a traction-free, horizontal, NS-oriented cylinder of 200 m total length. The cylinder's centroid is located exactly beneath the origin, a hydrostatic remote stress is applied equal to the gravitational stress $\sigma_{xx} = \sigma_{yy} = \sigma_{zz} = \rho g h$, where h is the depth to the cylinder centroid.

The DEM model displacements (U_x, U_y) as well as the displacement differences $(\Delta U_x, \Delta U_y)$ in Figure 5 match closely the Kirsch solution and the BEM results. For the Mindlin solution this is only true for the horizontal components. For the vertical components the modelled components only match the Mindlin solution in the near-field of the subsidence centre, while in the far-field a large disagreement is observable, expected from an intrinsic mathematical difficulty in determining the displacement of a stress-loaded half-space (Appendix B.3).
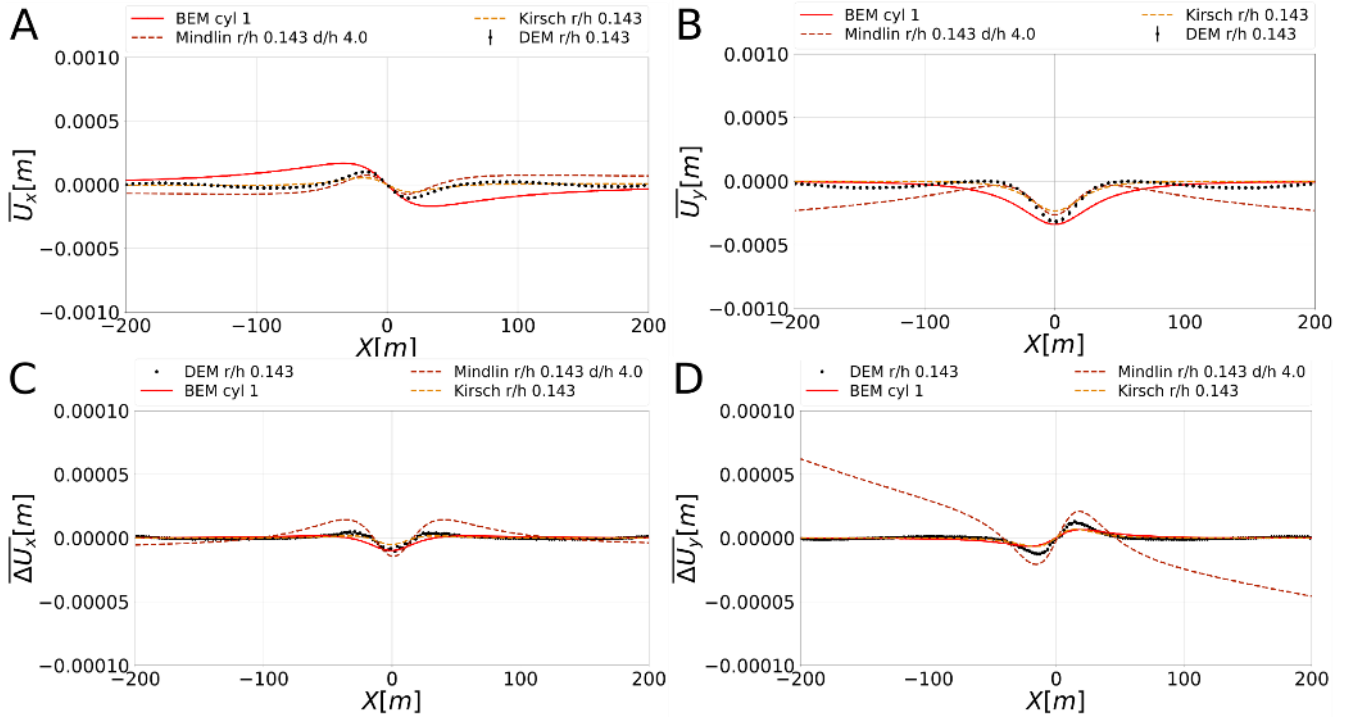
Figure 5: Results of benchmarking of the DEM cavity model against continuum-based cavity models: Analytical solutions and modelled displacement curves for model dimensions of 400 × 400 m with particle radius 0.32 m. Reference is a cavity with r/h = 0.143, at 35 m depth and with a 5 m radius. (A) Horizontal displacement, (B) vertical displacement, (C) horizontal displacement difference and (D) vertical displacement difference.

2.3 Model setup for cavity generation and sinkhole formation

Based on the above-described tests for model resolution, dimensions and cavity generation, a generalised setup for cavity growth with attendant fracturing and sinkhole collapse is presented in Figure 4C. This setup comprised a 400×400 m assembly of parallel-bonded particles of 0.32 m radius on average. The assembly is subdivided according to bond and particle contact properties into a cover material sequence that lies over a 'soluble' or 'mobile' material with a fixed basement rock below. The cavity is grown according to a material removal zone of arbitrary geometry, taken here as a vertically orientated half-ellipse, using the incremental deletion approach (M2) described above. For the technical details of the bond installation and void space creation procedure, see Appendix B.5.

A key geometric parameter in subsidence studies is the ratio of overburden thickness (T) to width or diameter (D) of the undermined area before the initiation of subsidence or collapse. In the following, T/D refers to: (1) thickness of the overburden / diameter of the cavity (T/D_{cav}) if materials can sustain a cavity in or around the material removal zone or (2) thickness of the strong material/diameter of the destabilised zone (T/D_{col}) if materials cannot sustain a cavity. This sub-surface destabilised zone is shown arbitrarily as a triangular shaped area in Figure 4C. For each model setup, at least two, mostly five different particle assemblies were run, and the errors in the following are based on these.

2.4 Calibration of Distinct Element Method approach for modelling sinkhole collapse at the Dead Sea

2.4.1 Bulk parameter estimation of geo-materials adjacent the Dead Sea

The geotechnical parameters of rocks and soils commonly cover a wide range, as they depend strongly on detailed mineral composition, grain sizes, external stress conditions, fluid saturation and stress histories, cf. e.g. *Brady and Brown,* [2006] and *Jaeger et al.,* [2007]. Here we consider geotechnical parameters for the three main material types involved in sinkhole formation at the Dead Sea region: (1) lacustrine clayey carbonates and evaporites, (2) alluvial sands and gravels and (3) pure rock salt (halite) (Table 2).

Table 2: Estimated geomechanical properties of main materials in sinkhole-affected areas at the Dead Sea. References are (Ezersky et al., 2017; Ezersky and Livne, 2013; Frydman et al., 2008, 2014; Hoek, 2007; Khoury, 2002; Manger, 1963; Polom et al., 2018; Zhu, 2010)**. *(T~UCS/10) after** *Hoek*, [1968]

Parameter	Symbol	Unit	Wet lacustrine mud	Alluvial sediment	Holocene Salt
Bulk density	ρ_{bulk}	[kg/m^3]	1500 - 2100	1500 - 2300	1400 - 2200
Porosity	n		0.2 - 0.3	0.2 - 0.3	0.05 - 0.4
Friction angle	ϕ	[°]	2.4 (wet) - 34 (saturated)	30 - 40	53
Young's modulus	E	[MPa]	83	220	300 - 10000

Poisson's ratio	ν		0.2-0.4	0.15-0.35	0.2-0.4
Unconfined compressive strength	UCS	[MPa]	-0.243 - -0.053	-5 - -0.1	-5 - -1
Unconfined tensile strength*	T	[MPa]	0.0053 - 0.0243	0.01 - 0.5	0.1 - 0.5
Cohesion	c	[MPa]	0 - 0.019	0.027 - 1.33	0.84 - 1.73 (at 20-40 m depth)

For lacustrine mud, friction angle, cohesion, porosity and density parameters from laboratory tests are used (Ezersky et al., 2013, 2017, Frydman et al., 2008, 2014). For the alluvial sediments, upper limits are given by nearby field investigations in firm sandstone rocks (El-Naqa, 2001) and also by published values for medium-grained Quaternary sand-gravel (Carter, 1983; Manger, 1963; Taqieddin et al., 2000). The bulk modulus of alluvial sand/gravel and lacustrine clays were estimated using Poisson's ratio values from the literature (Zhu, 2010) and shear-wave velocities from recent field measurements [*Polom et al.*, 2018], where the latter was reduced by a factor of 1.5 to account for drained conditions.

Elastic parameters and strength values of the field materials have been estimated by using tables from *Brown*, 1981 and *Hoek*, 2007 and by classifying the clayey mud as grade R0 in terms of intact rock consistency and the alluvial sediments as grade R0-R1 . The Holocene salt rock of the Dead Sea is considered weaker than typical halite rock salt (Frydman et al., 2008, 2014) and has been classified as grade R1. The cohesion value of salt is strongly depth dependent and has been determined by using depth-normalised results derived from triaxial tests (Frydman et al., 2014) via

$$c = \frac{q*z}{2*N_f} \qquad (1)$$

where $N_f = \sqrt{\frac{1+sin\phi}{1-sin\phi}}$, c the cohesion, z the depth of the rock sample, q the intercept in a principal stress $\sigma_1(\sigma_3)$ plot and ϕ the friction angle. We use a friction angle of $\phi = 54°$, depth $z = 20\text{-}40$ m and an intercept of $n = 259$ kPa for a specific rock weight of 18 kN/m³ (Frydman et al., 2014). For the alluvial sediment, we assume a friction angle of $\phi = 34°$ and an UCS of 0.1-5 MPa and calculate the cohesion value by the well-known relation $c = UCS/(2N_f)$ (Jaeger et al., 2007). Modulus, friction angle and strength hereby depend strongly on the porosity distribution, while the Poisson's ratio is quasi-independent of it (Schöpfer et al., 2009).

2.4.2   Calibration of DEM material properties via simulated rock tests

Bulk material parameters are determined by simulated, biaxial compression and tension tests similar to those described by *Khanal and Schubert,* [2005] and *Schöpfer et al.,* [2007] (cf. Figure 4B). We generated material 'samples' with dimensions of 10 x 8 m and with a mean particle radius of 0.32 m and an initial porosity of 0.2. Each sample then contains approximately
5   200 particles. In order to simulate the materials of the Dead Sea region, we used the micro-properties listed in Table 3 and the assembly generation scheme outlined in Appendix B5.1. Note that for the lacustrine mud material, we also implemented a re-bonding ('annealing') scheme to simulate the cohesiveness of that material. Tests were conducted with confining pressures p between 0 and -5 MPa, corresponding for a bulk density of ~ 2000-2200 kg/m^3 to depth range of 0 – 250 m. Measurement circles (averaging regions as described in *Potyondy and Cundall*, 2004) are installed in the centre of the sample to determine
10   the stress/strain and porosity values.

Table 3: Particle, contact and bond properties for DEM sinkhole collapse models. Note the geology convention

Parameter[3]	Symbol	Unit	Lacustrine mud	Alluvial sediment	Holocene Salt
Initial material porosity	n	-	0.2	0.2	0.2
Particle density	ρ	[kg/m^3]	2715	2750	2500
Contact Young's modulus[4]	E_L	[GPa]	0.1	0.2	1
Contact Young's modulus at particle-wall contacts	E_W	[GPa]	5	5	5
Bond Young's modulus	E_{Pb}	[GPa]	0.1	0.2	1
Bond tensile strength	$\acute{\sigma}_c$	[MPa]	0.1	0.5	1.0
Bond cohesion	$\acute{c}$	[MPa]	0.02	0.5	1.0
Bond friction angle	ϕ	[°]	2.4	34	54

The sand-gravel and salt materials show brittle failure behaviour (i.e. a sharp post-peak stress drop) at low confining pressures,
15   which changes to brittle-ductile behaviour for larger confining pressures (Figure 6). Ductile is defined as the state of deformation without significant loss of strength, and the transition to this behaviour is the brittle-ductile transition (Byerlee, 1968). The salty-mud material shows a brittle-ductile transition for all tested confining pressures, or more precisely, a brittle-to-cataclastic-flow transition to distinguish it from the brittle-to-crystal-plastic transition (Schöpfer et al., 2013).

---

[3] See Appendix A and *Potyondy and Cundall*, 2004, for a detailed definition of these parameters.
[4] A friction coefficient of 0.5 and a normal/shear stiffness ratio of 2.5 is chosen for all materials.
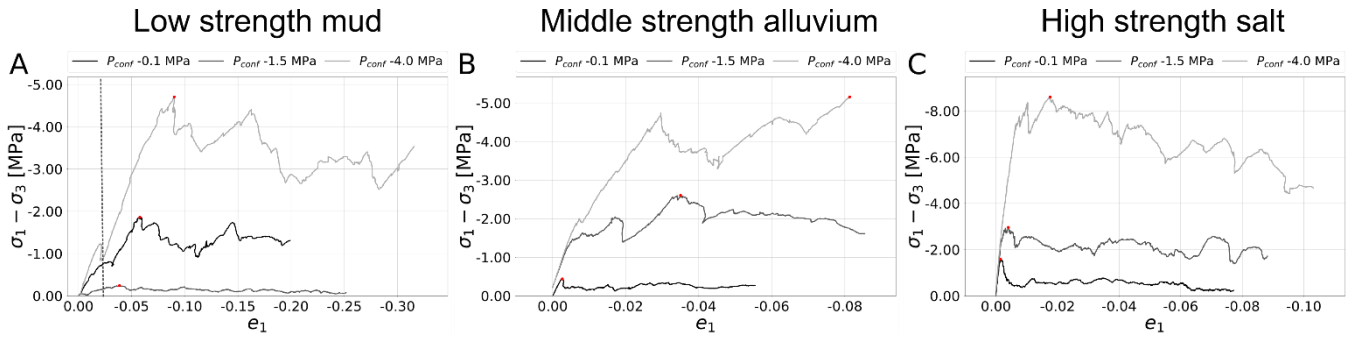
Figure 6: Differential stress versus vertical strain plots for simulated compression tests. Confining pressures of -0.1; -1.5 and -4.0 MPa are compared that highlight the depth-dependent division into elastic, yielding and post-peak behaviour in all tested materials: (A) Low strength lacustrine mud, (B) middle strength alluvial sediment and (C) high strength Holocene salt material. Black dashed line in (A) marks cut-off limit at E$_{yy}$ = -0.02 for lacustrine mud elastic properties and peak stress estimation.

Plots of the peak stress data for each confining pressure are used to estimate the bulk strength parameters according to the widely-applied Mohr-Coulomb and Hoek-Brown failure criteria (Hoek, 2007; Hoek et al., 2002; Hoek and Brown, 1997) (Figure 7). The Mohr-Coulomb failure envelopes for the compression tests are shown in Figure 7A. If tension test results are included, a highly non-linear behaviour of the material is recorded, so that a Mohr-Coulomb envelope is partly not appropriate anymore. Consequently, a non-linear Hoek-Brown envelope is included in Figure 7B, although it only fits well to all the data for the lacustrine mud material, and well to low-confining pressure data for the other materials.

The slopes of the elastic parts of the stress-strain curves are used to estimate the bulk elasticity parameters. Figure 7C shows that Young's modulus, E, increases with confining pressure (i.e. depth) and while Poisson's ratio, ν, shows no trend. Tensile tests reveal lower elastic moduli and Poisson-ratios than in the compression tests. An overview of the bulk material properties resulting from these calibration tests is given in Table 4. At low confining pressures, the failure envelopes for BPM are non-linear - cf. *Schöpfer et al.*, [2013]. Further details and examples are found in Appendix B.4.
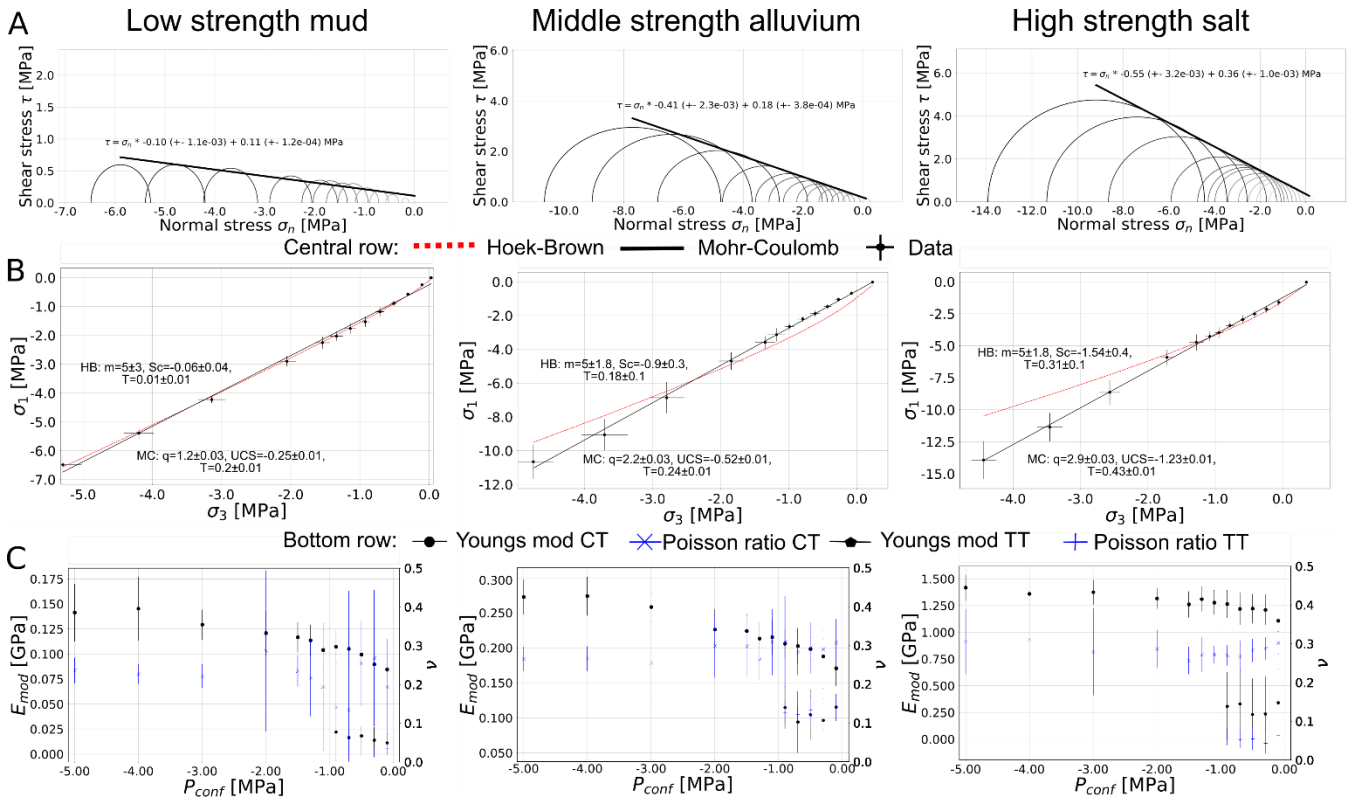
Figure 7: Bulk failure envelopes and elasticity parameters of the simulated Dead Sea materials derived from simulated laboratory tests. (A) Mohr-Coulomb failure envelopes, (B) Mohr-Coulomb and Hoek-Brown principal stress, (C) variation of elastic parameters with confining pressure. Left column: Low strength cohesive lacustrine mud, Central column: Middle strength alluvial sandy-gravel material, Right column: Higher strength Holocene salt. CT = Compression test data; TT = Tension test data.

Table 4: Bulk material properties of the three investigated Dead Sea materials as derived by simulated rock tests and measurement circles. All values refer to unconfined conditions (i.e. at or close to the surface). Mohr-Coulomb and Hoek-Brown results are based on compression and tension tests on ten different particle assemblies for each material.

Parameter	Symbol	Unit	Wet lacustrine mud	Alluvial sediment	Holocene Salt
Particle packing porosity	n_{eff}	-	0.21	0.2	0.17
Bulk density	ρ_{bulk}	[kg/m^3]	2145	2200	2075
Young's modulus	E_{eff}	[GPa]	0.084 ± 1.2^{-2}	0.174 ± 2.5^{-2}	1.106 ± 126^{-3}
Poisson's ratio	ν_{eff}		0.19 ± 0.12	0.31 ± 6^{-2}	0.30 ± 0.03
Mohr-Coulomb: Unconfined compressive strength	UCS	[MPa]	-0.25 ± 5^{-3}	-0.52 ± 8^{-3}	-1.23 ± 1.4^{-2}

Mohr-Coulomb: Unconfined tensile strength	T	[MPa]	0.2 ± 4^{-3}	0.24 ± 4^{-3}	0.43 ± 5^{-5}
Mohr-Coulomb: Cohesion	c	[MPa]	0.11 ± 1.2^{-4}	0.18 ± 5^{-4}	0.36 ± 1^{-3}
Mohr-Coulomb: Friction angle	ϕ	[°]	5.7 ± 0.06	22.3 ± 0.17	28.8 ± 0.18
Hoek-Brown: Unconfined compressive strength	UCS	[MPa]	-0.06 ± 0.04	-0.92 ± 0.28	-1.54 ± 0.41
Hoek-Brown: Unconfined tensile strength	T	[MPa]	0.01 ± 0.01	0.18 ± 9^{-2}	0.31 ± 0.14
Hoek-Brown: Ratio compressive/tensile strength	UCS/T	[MPa]	6.0	5.1	5

This calibration shows that the model materials mimic the mechanical responses of the natural materials, and it builds the basis for the analysis of the specific sinkhole formation problem at the Dead Sea, as presented in the following section.

3   Results of DEM models of void growth and sinkhole collapse

3.1   Development in 'end-member' Dead Sea materials

We simulated the effect of continuous material removal from a semi-elliptical subrosion zone at 20 m, 30 m or 40 m depth below the initial surface for all three end-member Dead Sea materials. For brevity we here report on the evolution of the models with subrosion at 30 depth only; for the detailed evolution of all simulated configurations, see the Electronic Appendix.

As shown in Figure 8 & Figure 9, the evolution of cavity development strongly depends on the mechanical interaction with the surrounding material. The mud is geomechanically the weakest end-member, and even the initial small cavity is not supported by it; the cavity collapses almost instantly after it is generated. Consequently, a cavity of large size (meter scale) never develops in the mud. As material is progressively removed from the subrosion zone, material from around and above the removal zone subsides gradually toward it. A column of subsiding material develops that is partly fault-bound and is characterised internally by downsagging of the overburden layering. This column grows upward until intersecting the surface, where a sag-like sinkhole forms. With further subrosion, the sinkhole grows deeper and wider as areas marginal to the subsiding column slump inwards.

In contrast, the alluvium is strong enough to sustain the cavity as it grows. The growing cavity interacts mechanically with the surrounding material, as sections of the cavity roof and walls collapse into it. Eventually, the overburden above the cavity fails abruptly, and the cavity is closed by the collapse of the overburden into it. The overburden collapse is also usually partly fault-

bound with downsagging or with a more complex internal structure. The resultant model sinkhole margins are characterised initially by large and deep (meter-scale) opening mode fractures (ground cracks), inward tilted blocks, and in part by overhanging sides. With further subsidence, the inward tilted blocks and overhanging sides tend to slump into the sinkhole's centre. The salt is the strongest end-member geomechanically, and so large stable cavities can develop within it - essentially
5   unaffected by deformation of the surrounding material - until only a thin 'bridge' of overburden is left.

The mechanical differences in the structural development are highlighted in Figure 9. For the low strength mud, stress arching, which tends to stabilise the overburden, is weakly developed around the material removal zone and within the overburden. Stress arching is well-developed around and above the cavity in the alluvium, although the absolute values of shear stress are
10   high on the cavity's lateral walls, suggesting that these areas are most susceptible to failure. The stress arch is disrupted upon final failure of the overburden and formation of a sinkhole. In the strong salt, stress arching is best developed and persists even after the thin 'bridge' of the remaining overburden fails.
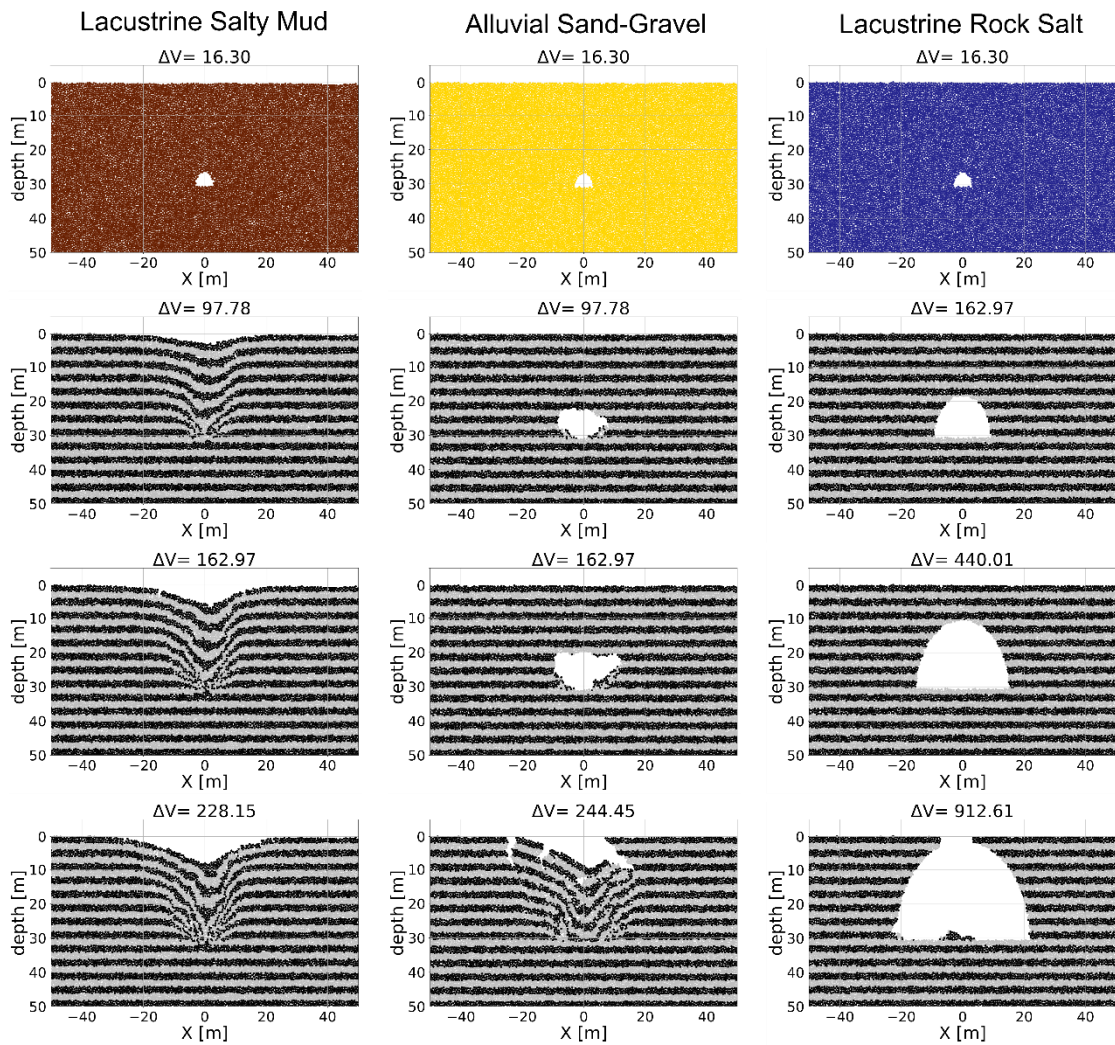
Figure 8: Evolution of DEM model cavity growth and sinkhole collapse in end-member Dead Sea materials. Shown here are selected stages in the development of cavity/sinkhole in salty-mud (left column), alluvium (middle column) and rock salt (right column). The top row shows the initial cavity growth stage for each material. The layering in the other rows defines passive markers and does not represent any change in material properties.
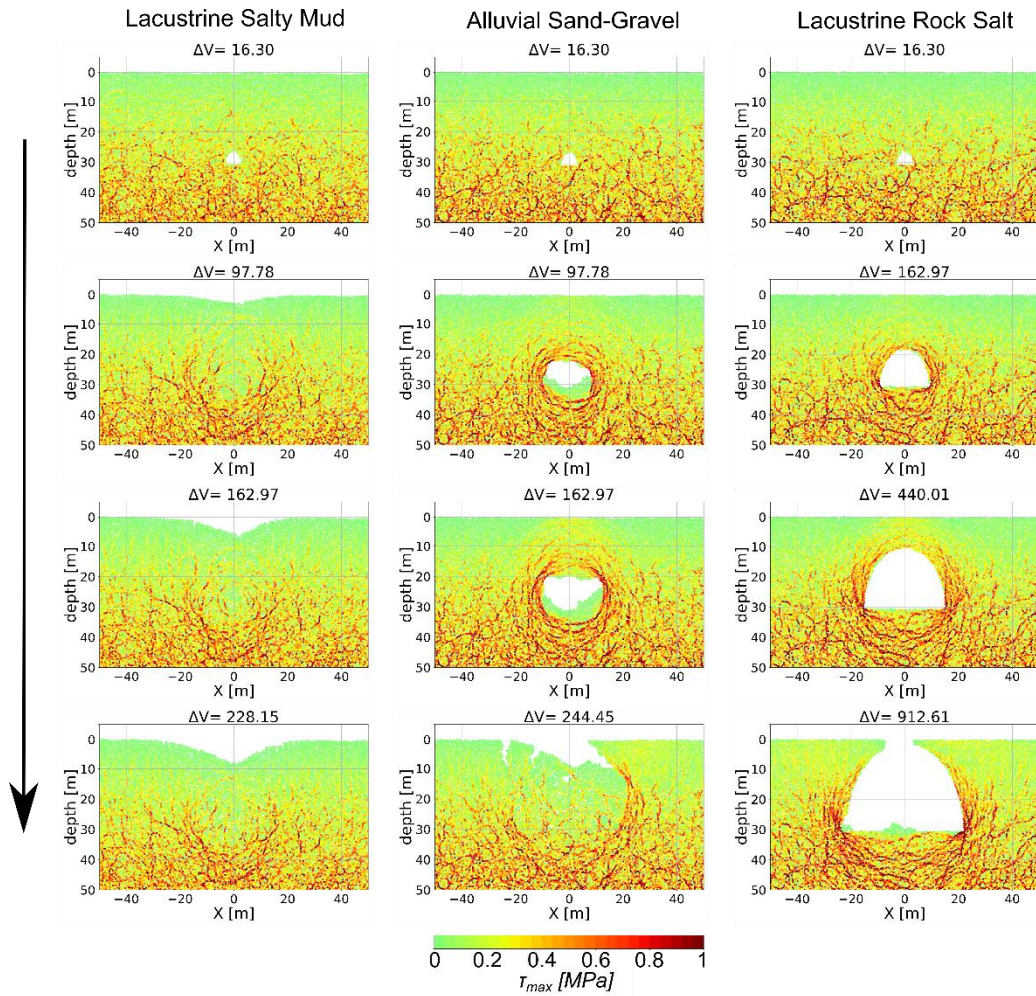
Figure 9: Evolution of maximum shear stress during cavity growth and sinkhole collapse in end-member Dead Sea materials. **Shown here are selected stages in the development of cavity/sinkhole in salty-mud (left column), alluvium (middle column) and rock salt (right column). Same model setups as in Figure 8.**

3.2 Development in layered Dead Sea materials

We also simulated the effect of continuous material removal from a semi-elliptical subrosion zone at 20 m, 30 m or 40 m depth below the initial surface for layered combinations of the end-member Dead Sea materials. The models comprise a layer of either alluvial sandy-gravel or rock salt (0 - 13 m depth) overlying a lacustrine mud layer (13 – 40 m depth) followed by the alluvium/salt as a basement, respectively. For brevity, we again report on the evolution of the models with subrosion at a depth of 30 m only (Figure 10 & Figure 11); for the detailed evolution of all simulated configurations see the supplementary electronic material.
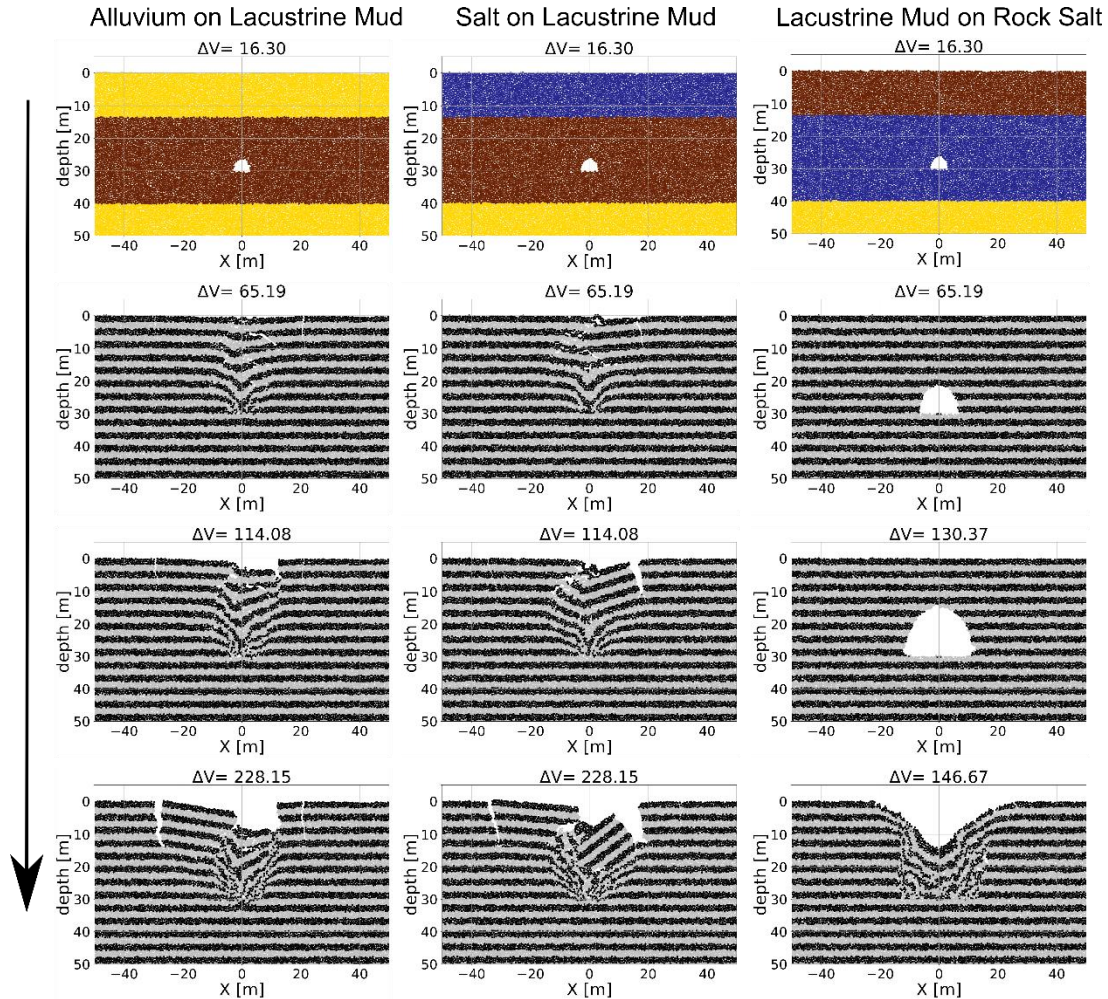
Figure 10: Evolution of DEM model cavity growth and sinkhole collapse in layered configurations of the end-member Dead Sea materials. Shown here are selected stages in the development of cavity/sinkhole in salty-mud overlain by alluvium (left column), salty-mud overlain by rock salt (middle column) and rock salt overlain by salty-mud (right column). The top row shows the initial cavity growth stage for each material. Note initial cavity again closes rapidly in the mud leading to a broader zone of subsurface instability.
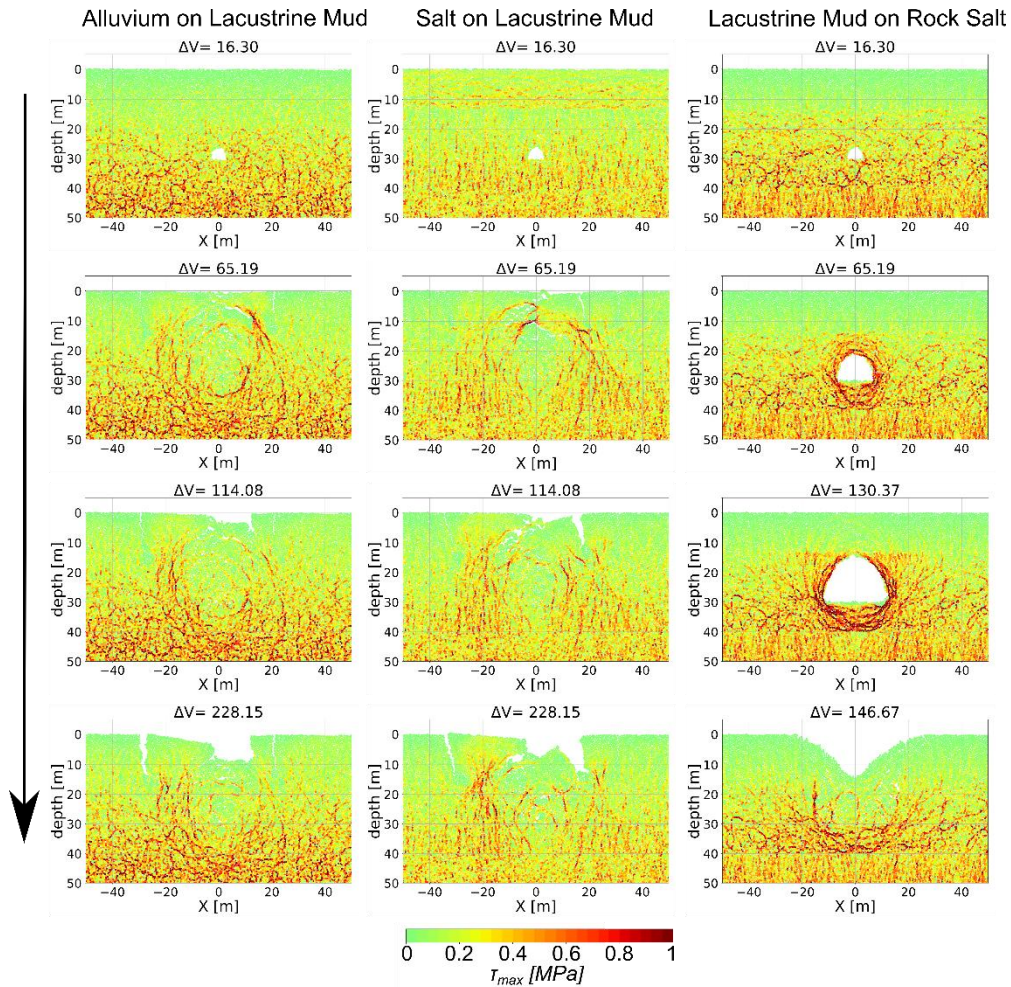
Figure 11: Evolution of maximum shear stress during cavity growth and sinkhole collapse in layered configurations of the end-member Dead Sea materials. Shown here are selected stages in the development of cavity/sinkhole in salty-mud overlain by alluvium (left column), salty-mud overlain by rock salt (middle column) and rock salt overlain by salty-mud (right column). Same model setups as in Figure 10.

In general, for layered materials with mud as the subrosion-affected interlayer, the ground tends to fail clearly earlier than for the uniform materials. The mud cannot sustain large cavities and hence fails immediately upon material removal, and the upper mud layers bend. This leads consequently to the development of a cone-shaped underground collapse zone. In alluvium on lacustrine mud, a small subsidence may be noted before collapse and cracks appear even at a certain distance from the main area. Note also the development of ephemeral cavities at the interface with the mud, and/or within the alluvium or salt top layers, as deformation migrates upward toward the surface. After the collapse, large and small rotated blocks slump towards the centre, and opening cracks grow downwards to a depth of 12 m around the collapse zone. These blocks define the base of the formed sinkholes. Although salt has double the strength of alluvium, the shapes of the sinkhole for these multilayer models

do not differ much, but a small tendency to more overhanging sides is observed. For the condition of lacustrine mud on rock salt, the salt layer sustains large cavity formation, but as soon as the void space reaches ~2 m below the mud-border, the material collapses. The formed sinkhole is a mixture of typical endmember types mentioned in Section 1.

5   As shown in Figure 11, the mechanical effect of the weak mud layer is to inhibit the development of stable stress arching in the overburden. Where the weaker layer lies below the stronger layer, the development of a collapse zone is indicated as a zone of low stresses, around and above which a stress arching is weakly developed. Effectively, this subsurface collapse zone is mechanically similar to a large cavity. The lack of support from the weak layer concentrates stress in the stronger layer (note the high magnitude of shear stress there), pushing the strong layer toward failure. Where the weak layer overlies the strong 10   layer, the stress arch is well developed until the cavity growth nears the weaker layer. The weaker layer cannot sustain the stress arch, and so the overburden collapses.

3.3   Effect of subrosion zone depth

As shown in Figure 12, the variation of depth of the subrosion zone changes the morphology of the sinkholes. For more details 15   refer to the Electronic Appendix. The removed material in the subrosion zone is assigned a removed "volume" ΔV, which is based on the area of the removed disc shaped particles and its unit thickness, cf. Appendix A.
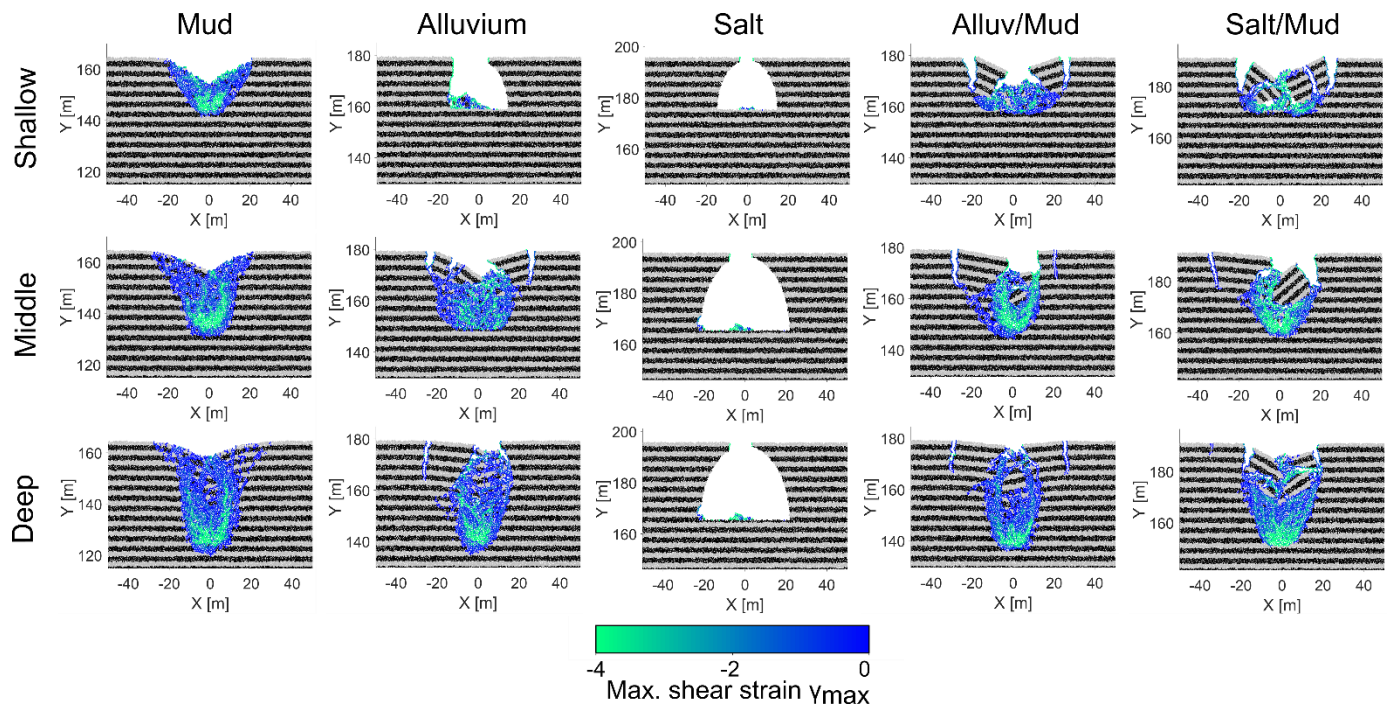
Figure 12: Sinkhole endmembers in dependency of the depth of the subrosion zone for all material combinations investigated in this study. The maximum shear strain is used to visualize the collapse zone.

In lacustrine salty-mud, for all subrosion depths, the sinkhole collapse is gradual with continuous subsidence. The deeper the subrosion zone, the lower the vertical displacement at the surface and a greater amount of material need to be removed before an effect is visible at the surface ($\Delta V \sim 80$ m^3 for deep vs. $\Delta V \sim 50$ m^3 for shallow). For a shallow subrosion zone, the sinkholes are V-shaped with partly steep margins. For middle subrosion zones the sinkholes exhibit a compressed V-shape with both flat and steep margins. In contrast, the deep subrosion zone leads to bowl-shaped sinkholes with flat sides.

In the homogeneous alluvium models, the sinkhole collapse process varies between sudden (shallow material removal zone) and partly gradual (deep zone). For a shallow subrosion zone, the collapse occurs relatively late at a removed material volume of $\Delta V \sim 400$ m^3. A long-term stable cavity, also asymmetric (cf. Figure 8) can reach the immediate subsurface, and no precursory cracks at the surface appear. The final sinkhole is A-shaped with overhanging sides. A deep subrosion zone causes cracking in the overlying layers and at the surface together with subsidence before gradual collapse occurs, commencing relatively early at $\Delta V \sim 80$ m^3. The final sinkhole is V-shaped.

In homogeneous rock salt models, for all subrosion depths the sinkhole collapse is sudden and occurs after large amounts of material are removed. The sinkholes that form are in all cases A-shaped. No surface subsidence can be observed before the collapse, as the void spaces stay stable up to the immediate subsurface. For a shallow subrosion zone the cavity fails very late

at $\Delta V \sim 400$ m3, for a middle subrosion zone at $\Delta V \sim 900$ m3 and for a deep subrosion zone at $\Delta V \sim 1500$ m3. The latter shows pronounced spalling at the sides of the cavity. The shallow model only fails because the material left is of minute thickness.

5 For the multilayer model alluvium on mud with alluvial basement, the collapse in all cases happens earlier than in pure alluvial material and is sudden. For a shallow subrosion zone the sinkhole forms at $\Delta V \sim 240$ m^3, for a middle and deep subrosion zone at $\Delta V \sim 80\text{-}100$ m^3, with little subsidence before collapse onset. For middle and deep subrosion zones the formed sinkhole is initially narrower but widens with continued material removal. For the shallow zone, this does not happen due to lack of material.

Similar features are observed for the multilayer model salt on mud, the collapse in all cases happens earlier than in pure salt material and is sudden. The removed volume before collapse is similar to results from alluvium on mud, namely for a shallow subrosion zone the sinkhole forms at $\Delta V \sim 240$ m^3, for a middle and deep subrosion zone at $\Delta V \sim 80\text{-}120$ m^3, with little pre-collapse subsidence and compression ridges. The sinkhole morphologies are similar to the ones for alluvium on mud, but a

15 tendency to larger block size and a more pronounced overhanging is observed.

3.4   Thickness to diameter ratio at the onset of collapse

Figure 13A shows the estimated T/D ratios at the onset of the collapse (T/D$_{crit}$) for all model setups independent of the subrosion zone depth. A collapse hereby is defined when both particle movement at the surface and in the subsurface occurs. A distinction for the different involved materials is found. Pure lacustrine mud models generally fail at higher ratios $T/D_{crit} \geq$

20 0.5 than the majority of the other models. Multilayer models with mud underlying alluvium or salt show low $T/D_{crit} \leq 0.5$, while pure alluvium or salt models have the highest and lowest measured values, respectively. A collection of the mean values is given in Table 5. The deeper the subrosion zone in both multilayer and uniform material models, the less material needs to be removed to trigger a collapse (Figure 13B).

25 **Table 5: Critical thickness to diameter ratios for modelled sinkhole collapse onsets. The error is based on the mean between different particle assemblies for each setting.**

Subrosion zone depth/Modelled material setup	Lacustrine Mud	Alluvium	Salt	Alluvium on mud	Salt on mud	Mud on salt
Shallow	0.66 ± 0.01	0.06 ± 0.05	0.02 ± 0.01	0.22 ± 0.05	0.17 ± 0.1	-

Middle	0.57 ± 0.05	0.5 ± 0.29	0.03 ± 0.03	0.32 ± 0.08	0.48 ± 0.15	0.43 ± 0.1
Deep	0.57 ± 0.02	0.97 ± 0.1	0.08 ± 0.01	0.27 ± 0.06	0.51 ± 0.03	-
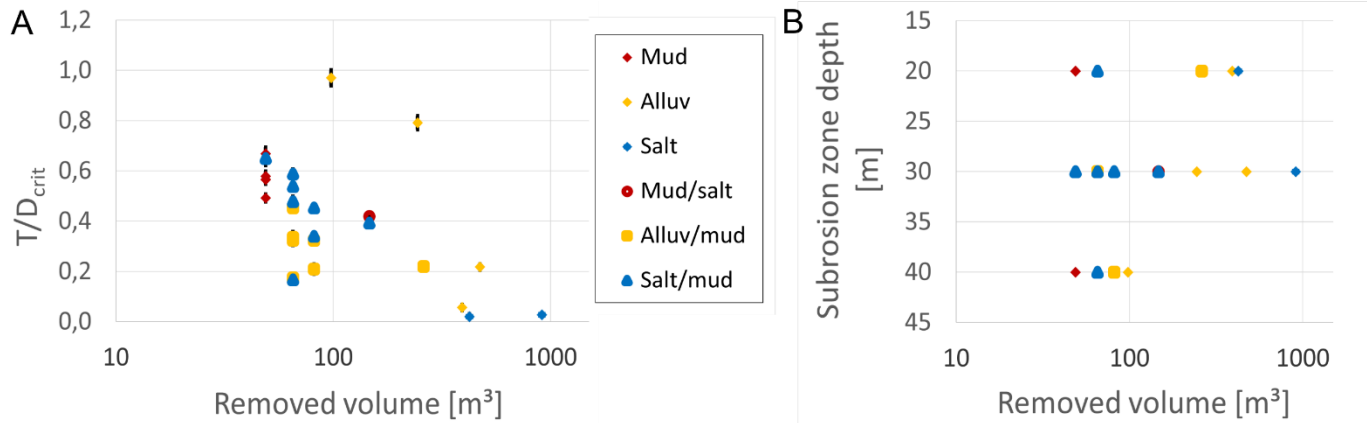
Figure 13: Parameters at the onset of collapse. (A) Thickness to diameter ratio versus removed volume at the onset of collapse. Note that the T/D$_{crit}$ ratio is either referring to the (stable) subsurface cavity or the (instable) subsurface collapse zone. Reddish colors stand for mud, orangish for alluvial material and blueish for salt and the respective multilayer models. (B) Removed volume at the onset of collapse in dependency of the subrosion zone depth.

4   Comparison with data derived from photogrammetry at Ghor Al-Haditha sinkhole site

4.1.1   Surface displacement

In Figure 14, we compare the topographic profiles of sinkholes derived from photogrammetric studies at Ghor Al-Haditha (cf. Section 1, Figure 3) with our results from DEM sinkhole modelling. In Figure 14a, we show the simulated sinkhole morphologies for different evolution stages for a subrosion zone with intermediate depth (30 m). To facilitate the comparison, the topographic profiles derived by photogrammetry have been normalized and the axes have been adjusted to the same dimensions as for the models (Figure 14B). An impressive similarity can be found for these sinkhole end-members both in terms of lateral extent and subsidence amplitude: (1) the mud sinkhole in the field appears to be of an early stage sinkhole but with a larger extension laterally; (2) the alluvium sinkhole shape is remarkably similar to the late stage (evolved) modelled sinkholes both laterally and vertically; (3) the salt sinkhole is comparable to the respective simulation result for an early stage salt sinkhole.
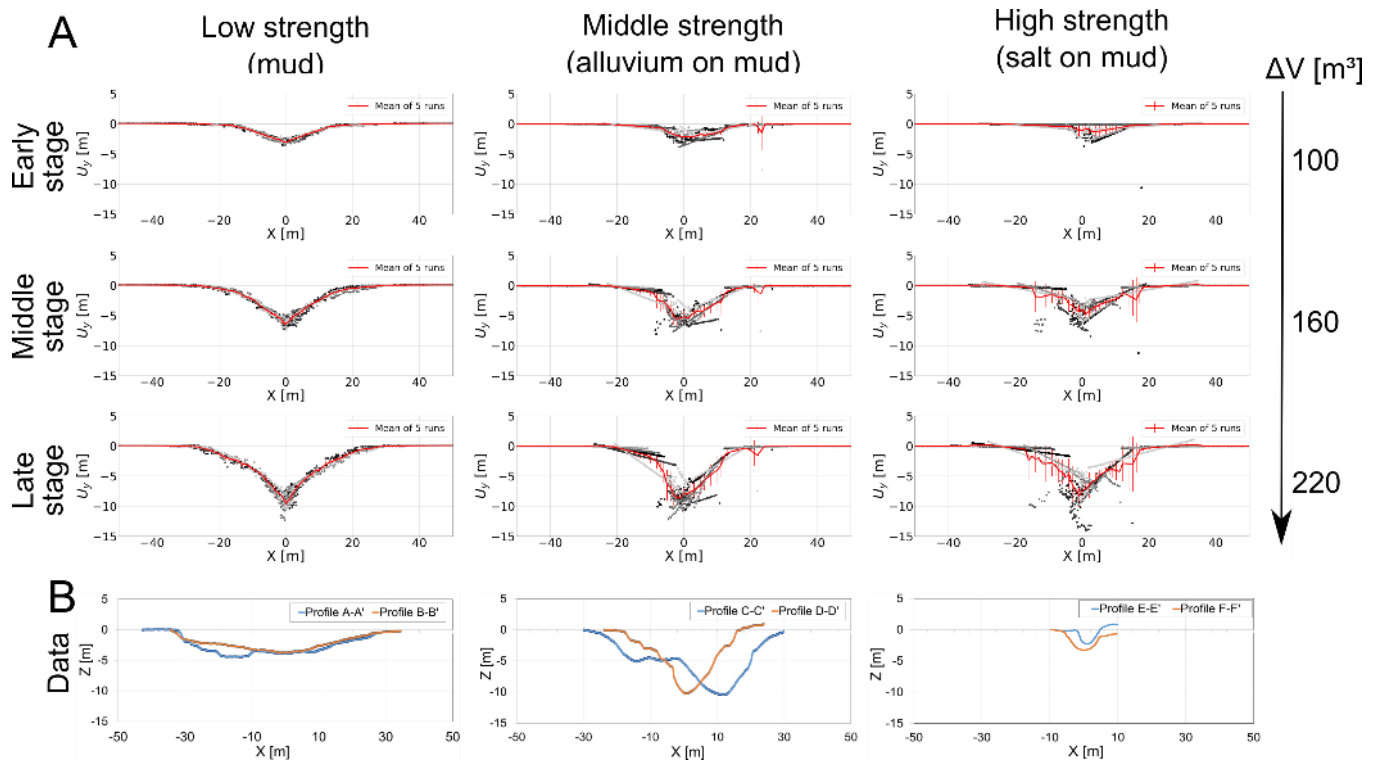
Figure 14: Topographic cross-sections of sinkholes in different cover materials. (A) Modelled profiles for subrosion zones in 30 m depth and three different evolution stages. Plotted is the vertical position of the surface particles for 5 different particle assemblies of each tested model setup. Model sets are: pure lacustrine mud (left row), alluvium on mud multilayer (middle row) and salt on mud multilayer (right row). (B) Field data replotted topographic profiles of the three different sinkhole morphologies from Figure 3. The distance and altitude are normalized for better comparison with the models.

These findings are essentially confirmed by knowledge about the rather recent development of the sinkholes selected in the mud- and salt-flat and the older, more evolved sinkholes in the alluvial fan of Ghor Al-Haditha (Al-Halbouni et al., 2017). Our models, which are based on realistic material parameter estimation, hence reproduce the topographic features of the sinkholes successfully in the field site. This result is even better reflected in the De/Di analysis described in the following section.

4.1.2   Sinkhole depth/diameter ratios

In Figure 15, we compare the sinkhole depth to diameter (De/Di) ratios for the DEM models and for natural equivalents at the Ghor Al-Haditha field site Ghor Al-Haditha based on. We use results from the models with uniform lacustrine mud from the layered models of alluvium on mud for different stages of collapse (early, middle and late). Figure 15 does not include data for salt-on-mud layered models, as natural equivalents were not mapped by *Al-Halbouni et al.*, [2017], but the De/Di ratios for these models are given in Table 6 and are generally similar to those in alluvium-on-mud models. Mean values of De/Di are 0.37 $\pm$ 0.15 for alluvium, 0.15 $\pm$ 0.02 for mud and 0.33 $\pm$ 0.11 for salt and close to the statistical estimates given by *Al-Halbouni et al.*, [2017], and to the examples shown in Figure 2.

In simulations with uniform mud material, the fit to the De/Di data is good in the early and intermediate stages of collapse (Figure 15a). For the late stages of these models, the model De/Di ratios are at the outer bound of the natural range. Conversely, in simulations with alluvium-on-mud material, the fit to the De/Di data is better in the intermediate and early stages of collapse (Figure 15b). For the early stages in alluvium, the results are at the lower margin of the depth.
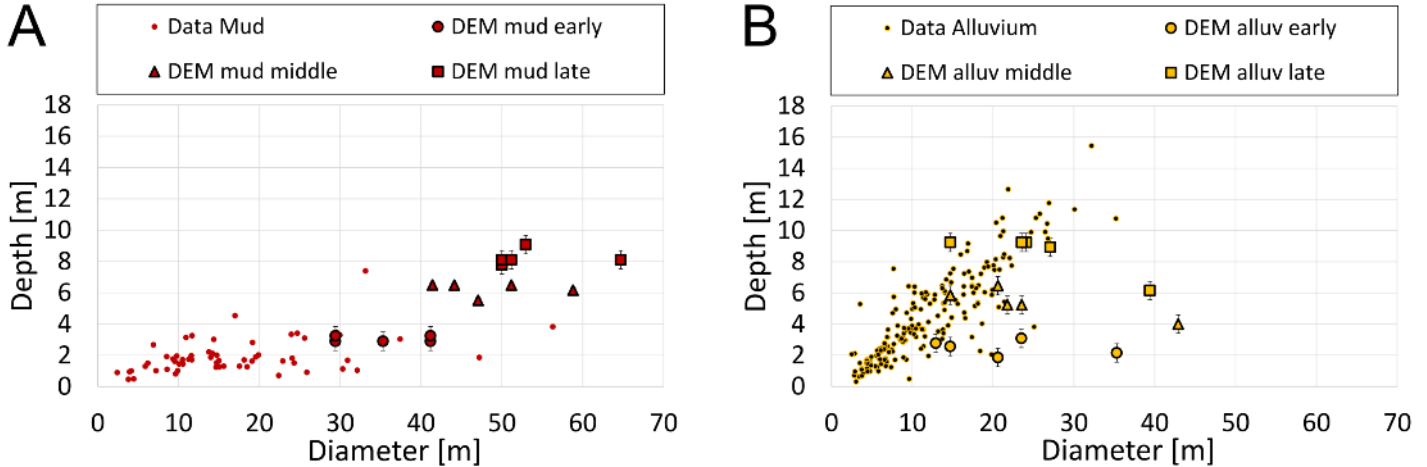
Figure 15: Sinkhole depth to diameter ratios from photogrammetry (Al-Halbouni et al., 2017) **and DEM model results of this study. For field data, depth and diameter for the materials alluvium and mud were determined for 237 sinkholes. The mean values are 0.4 ± 0.11 for sinkholes in alluvium and 0.14 ± 0.04 for those in mud. No field data was available for salt at the time of this study. For the models, we distinguish between early collapses (circles), middle collapses (triangles) and late collapses (squares). (A) mud-flat sediments and lacustrine mud models, (B) alluvial sediments and multilayer alluvium on lacustrine mud model results.**

Table 6: Depth to diameter ratios for modelled sinkhole collapses. A set of 5 models for each material combination is analysed for a subrosion zone at middle depth (30 m). De/Di ratios for alluvium and salt are generally higher than for mud.

Collapse stage	Removed volume [m³]	Lacustrine mud	Alluvium on mud	Salt on mud
Early	100	0.09 ± 0.01	0.13 ± 0.06	0.08 ± 0.05
Middle	160	0.13 ± 0.02	0.25 ± 0.1	0.21 ± 0.08
Late	220	0.15 ± 0.02	0.37 ± 0.15	0.33 ± 0.11

5   Discussion

5.1   Comparison to previous DEM and non-DEM studies of cavity generation and sinkhole collapse

Baryakh et al., [2008, 2009] used the DEM to investigate the effect of depth, geometry and mechanical properties on the collapsed state in karst. Their approach is to some extent similar to ours, however, essentially only the position of a rectangular or an arched cavity was varied for different uncalibrated materials. In contrast, our numerical simulations allow for a mechanical interaction of a slowly growing void space with the surrounding rock and provide calibrated bulk rock parameters. Consequently, the material removal either creates a cavity or not, leading to variably shaped subsurface collapse zones, details

of which are elaborated later. *Hatzor et al.*, [2010] used jointed blocky rock mass (DFN) modelling to define stability criteria (T/D ratios) for a rectangular cavern in high strength (UCS > 10 MPa) rocks. One conclusion of their study, namely the conservative T/D = 1.0 for large cavity sizes, may also apply to our results for homogeneous, relatively weak rock and cohesive soil models. Nevertheless, the stability depends strongly on the collapse zone geometry, and the well-known stability limit for

5 deep-seated excavation from (Terzaghi, 1946) does not hold for our shallow collapse zones. A FEM approach from *Shalev and Lyakhovsky*, 2012, addresses sinkhole formation by utilizing visco-elastic rheology with a damage model. It is applied to the sinkhole hazard at the Dead Sea and relates the different deformation modes (visco-elastic vs. brittle) to the different mechanical properties of the involved materials (mud vs. alluvium) and their common morphological characteristics. However, no field data comparison is given, and sinkhole formation is only simulated using a simplified cavity geometry that does not

10 evolve.

In summary, earlier studies lack a detailed calibration of the model strength parameters to field and laboratory estimates, and quantitative comparisons of model results with measured data are limited or absent. Our study hence fills this important gap and explicitly simulates cavity growth and related sinkhole development and therefore provides a significant advance in this

15 field.

5.2   Model testing, and benchmarking and limitations

Our tests and model benchmarking provide several new insights for undertaking the simulation of karstic void development and sinkhole collapse under gravity with the DEM. As expected there is a strong sensitivity of model results (displacement) not only to parameters such as model dimensions and resolution but also to model shape, with the best results attained for

20 relatively high resolution and equidimensional model set-ups. Our tests also show that the method of cavity generation has only a minor impact on the surface displacement pattern. Cavity generation by particle deletion differs from generation by particle radius reduction mainly in the much longer model runtime for the latter. This is reasonable given the elastic and quasi-static conditions of the DEM test models. By such tests, we infer that the models with non-elastic deformation (i.e. cavity wall failure and sinkhole collapse) are also insensitive to cavity generation method as long as they are run under quasi-static

25 conditions, as was the case in our study.

In the benchmarking tests, the DEM surface displacements for a circular cavity in a gravitationally-loaded elastic material closely resemble those predicted by the BEM model and the Kirsch solution both in the far- and near-field of the subsidence centre (cf. Figure 5). A perfect match is not expected, despite our efforts to compare like-for-like, having in mind the intrinsic

30 differences between these models in terms of material properties and boundary conditions. The Kirsch results nonetheless provide the best match to the DEM results for both vertical displacement and displacement differences. Overall, the DEM and Kirsch curves fit in the near-field and behave similarly and realistically (tendency to zero) in the far-field. The BEM models offer a plane-strain solution for a hydrostatic remote stress, while the two-dimensional DEM model does not consider out-of-

plane stress/strain and additionally has before cavity creation a horizontal to vertical stress ratio K_0 equal to $\sim 1/4$. This leads to the generally narrower vertical and horizontal displacement curves in the DEM models at the centre of the subsidence area. The mismatch to the Mindlin solution is greatest in the far field displacements; these displacements as predicted by the Mindlin solution seem are unrealistic given that they progressively increase away from the cavity. Consequently, for the purposes of this work and in light of the minute differences between the DEM results and the BEM/analytical solutions (sub-millimeter for displacements and micrometer for displacement differences, except for the Mindlin solution in the far-field), we consider the DEM model approach here to be a valid numerical approximation of the problem.

The manner of cavity growth and its timing relative to collapse are, of course, simplified approximations to complex processes of dissolution and mechanical erosion of the subsurface as they occur in nature. The model cavity grows by instantaneous and repeated material removal of the same volume within a domain of simplified shape. In reality, cavity growth may occur on extremely long to relatively short timescales, depending on the nature of the materials (e.g. limestone vs salt) and hydrogeological conditions (e.g. porous flow, conduit flow, dripping, flash floods). The cycling to quasi-static equilibrium during each model growth increment ensures, however, that cavity growth rate is smaller or equal to collapse rate, as expected in nature. An improvement will be to adjust the cavity area growth function to follow typical dissolution laws (cf. *Dreybrodt and Kaufmann*, [2007], *Kaufmann and Romanov*, [2015]) and thus to develop more complex and realistic cavity geometries.

5.3 Geomechanical parameter calibration

The outcomes of the simulated compression and tension tests (Table 4) closely agree with literature values and estimations from geotechnical studies and seismic velocity measurements (Table 2), in terms of UCS ranges, bulk densities, Young's modulus and Poisson ratios. The friction angles of the simulated sand-gravel and rock salt materials are slightly lower than the desired values, but fit well in case of the low strength lacustrine clay material. Low friction angles are typical for bonded particle models (cf. e.g. *Schöpfer et al.*, [2017]), because both sliding and rotation of particles accommodate bulk deformation; with the contact model used in the present study the latter cannot be inhibited even with large friction coefficients. It is well known from other DEM studies that UCS/T ratios in bonded-particle materials are lower when compared to natural rock (UCS/T~10) and soils (UCS/T ~8, (Koolen and Vaandrager, 1984), reflecting the discretisation by means of circular/spherical particles [*Schöpfer et al.*, 2007, 2009].

The Mohr-Coulomb and Hoek-Brown failure envelopes (Figure 7) fitted to the calibration data serve as guides to the material behaviour. These envelopes were chosen as they are widely used in geomechanics, and so the overall behaviour of the model materials is readily assessed from them. In detail, however, neither envelope provides a perfect fit to the calibration results. This may a consequence of the timing of confinement of the particle assembly, which is here done before installing the parallel bonds. Our results indicate that this may lead to some stress-path dependent behaviour that is more complex than can be

represented fully by either Mohr-Coulomb or Hoek-Brown envelopes. A thorough exploration of such complexities is well beyond the scope of this paper, but it could be subject of future work.

It is well known that the relationship between field-scale rock parameters and those determined at the laboratory sample scale depends strongly on the degree of fracturing or alteration of the rock mass (Schultz, 1996). Given that the materials we studied are of rather low-strength and are weakly consolidated materials (in contrast to hard karst rock in which sinkholes often form), we neglected the effect of pre-existing weaknesses (e.g., tectonic fractures). We hence adopted literature values for salt and mud derived from laboratory-scale measurements. A poorly understood effect in the Dead Sea materials is, however, the influence of water content which may lead to time-dependent geomechanical behaviours (see *Shalev and Lyakhovsky*, [2012]) that is not accounted for in our models. In principle, however, the modelling scheme we developed could be adapted to account for time-dependent (e.g. visco-elastic) material behaviour.

5.4   General implications for cavity and sinkhole formation

5.4.1   Structural or morphological features of sinkholes

The DEM models of sinkhole collapse show a wide range of structural or morphological features that are found at natural sinkholes, and they highlight how these features reflect the mechanical properties of the material in which the sinkholes form. Similar near-surface structural features are found at volcanic collapse calderas and pit-craters, and similar explanation in terms of mechanical properties of the near-surface materials have been proposed (Holohan et al., 2011; Poppe et al., 2015).

In relatively weak materials (here the simulated 'mud'), the near-surface strain is distributed across many small fractures, such that there is no sharp margin to the sinkhole. Subsidence at the surface develops gradually before the collapse develops (if at all) and the material's response is brittle-ductile. The sinkhole also widens gradually as it deepens. Overall, the sinkhole formation process is similar to classic 'cover sagging' or 'cover collapse' with partial suffusion (cf. *Gutiérrez et al.*, [2008]).

In relatively strong materials (here the simulated 'alluvial sand-gravel' and 'salt'), the strain is localised on fewer but larger fractures that develop as faults (shear fractures) and/or deep cracks (opening-mode fractures). Structures like compression ridges form in the centre of the subsidence area. Sinkhole margins in such materials are consequently sharp, steep, and, at least initially, overhanging. Any subsidence before collapse is slight, although this depends partly on material rigidity (i.e. modulus); the material's response is brittle. The sinkhole also widens as it deepens, but in more of a step-wise manner as new marginal fractures form and delimit marginal blocks. Overall the collapse style is similar to classic 'caprock collapse' or 'bedrock collapse' (see *Gutiérrez et al.*, [2008]). In extremely strong materials, there may be little or no collapse at all - in the limit the hole may result simply from the intersection of an essentially-stable, growing cavity with the ground surface.

5.4.2 Stability of cavities and relationship to sinkhole geometry

The stability of cavities in the DEM models is clearly related to the strength of the material and to the depth of the material removal zone. In general, the cavity stability depends on a combination of material strength (UCS, T, friction coefficient) and geometric properties (cavity geometry, T/D ratio). In principle, larger T/D and stronger materials promote larger void spaces in the underground as stable compression arches build up (Figure 16, see also *Holohan et al.*, [2015]). Thus for a given T/D, cavities are unstable in the weak 'mud' material but are stable in the stronger 'sand-gravel' and 'rock salt' materials. As the cavity grows, however, the T/D ratio decreases and ultimately the overburden geometry can no longer support its weight. Eventually, the overburden will fail partially or completely and collapse into the cavity.
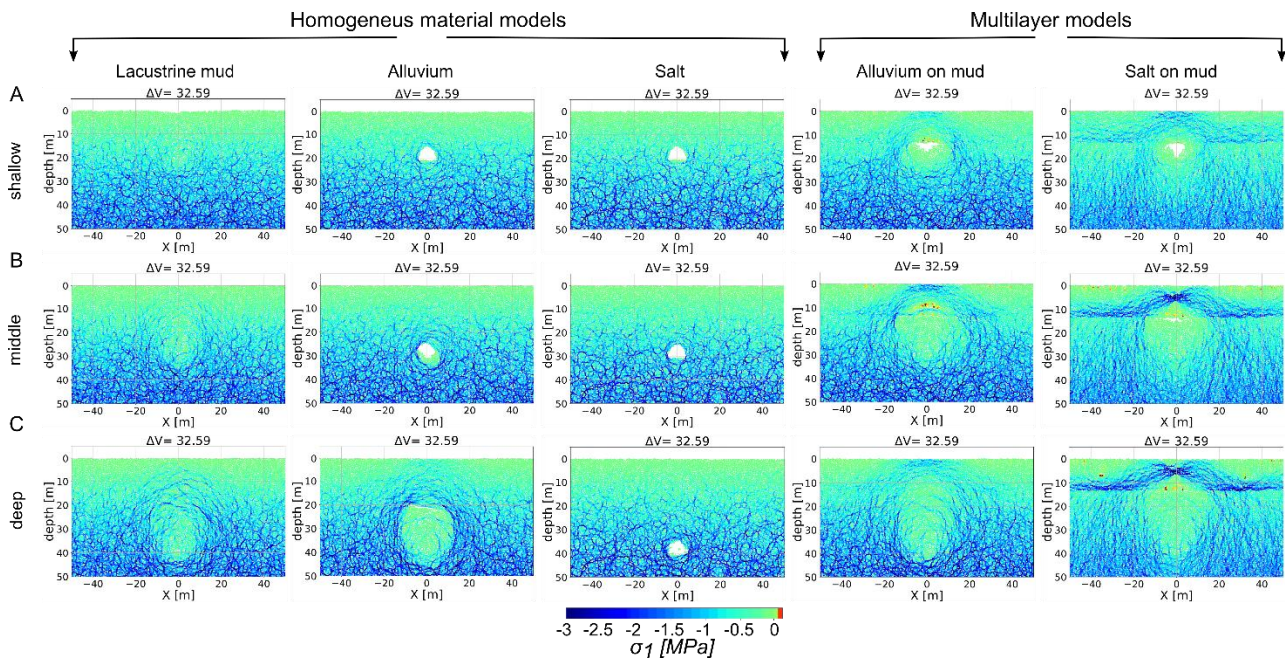
Figure 16: Maximum compressive stress for representative models after the same amount of material removal (~ 33 m³). Different depths of subrosion zones are compared: (A) shallow (20 m), (B) middle (30 m) and (C) deep (40m). The deeper the zone, the higher the maximum compressive stress above the created void space. The stronger the material, the more pronounced is the compression arch. Tensile stresses are observed directly above the removal zone.

The gravitational stress field in the models also means that the absolute depth, and not just relative depth as expressed by T/D, is critical, however. The deeper the cavity, inside which stresses are zero, the higher the differential stress immediately around it (Figure 9Figure 11 &Figure 16). This accounts for the observation in our models that for a given material strength, deeper-seated cavities fail earlier than shallow ones in these weakly consolidated materials. Overall our results indicate that cavity sizes and stability, and hence the style of sinkhole collapse, will depend on the material strength and depth of dissolution. Thus caprock collapse sinkholes, which form above large cavities (Figure 1), may be favoured for relatively strong material and/or shallow dissolution levels. Dropout or suffusion sinkholes may be favoured by relatively weak material and/or deep dissolution

levels. In the limit, no macro-scale cavities will form below a certain dissolution zone depth in a given material, as in-situ stresses become too high for that material to support such cavities.

The DEM models also show how the interaction of material removal and mechanical instability can lead to cavity growth. This
5 is seen mainly in moderately strong DEM material (here the 'sand and gravel'), where void spaces usually stay stable until large volumes of material are removed, with typical spalling at the sides rather than from the roof (Figure 8). This lateral spalling of the cavity is typical of "tunnel breakouts" encountered by engineers and arises from the in-situ stress field in the DEM model surrounding the cavity being characterised by a $K_0 < 1$ ($\sigma_{xx} < \sigma_{yy}$). In nature a feedback mechanism may arise from such spalling, whereby lateral or vertical spalling expose more fresh surfaces to dissolution and reduces the overburden
10 T/D, leading to further cavity growth and instability, leading to more spalling, etc.

Another important result of our DEM models is that multilayer models with a weak (mud) interlayer fail earlier than the models with a uniform material. This is not only because the integrated strength of the overburden is lessened, but also because the rapid failure of any cavities in the weak layer effectively increases the stress concentration in the strong overlying layer, similar
15 to a beam (Figure 16), leading to bending induced stresses with inner arc contraction and outer arc extension. This is contrary to the higher T/D ratios for the same amount of removed volume in the homogeneous layer models in which a stable cavity develops.

A consequence of such material-controlled cavity stability is that, as is often inferred for nature (e.g. *Waltham et al.*, [2005]),
20 the geometric relationship between sub-surface cavities and sinkholes is not a straightforward one. In the weak DEM model material, a sinkhole can have little or no geometric relationship to a cavity, because cavities are not sustained at any comparable scale. In the strong DEM model materials, on the other hand, the sinkhole geometry may relate to cavity geometry to a variable degree. This relationship may be especially direct in the case of a shallow removal zone and a very strong material, where a cavity can stably grow upward with little or no collapse until intersecting the ground surface. Overall, our results reinforce the
25 point that the use of continuum based methods to estimate cavity geometry from sinkhole geometry (i.e. where there are large permanent strains) should be treated with caution (see also *Fuenkajorn and Archeeploha*, [2010] and *Holohan et al.*, [2017]).

Future work will include a variation of lateral (long-wall mining like), vertical (tube-like), and multiple void space growth systems. Especially, for typical karst simulations, multiple void spaces with different growth functions and geometries are a
30 more suitable, complex approach. Another aspect is the role of hydrostatic (buoancy) and pore pressure, which is usually an important factor regarding soil liquefaction and landslides due to the reduction of effective stress (cf. e.g. *Tharp*, 1999; *Zeev et al.*, 2017; *Clément et al.*, 2018) and has been ignored in these simulations for simplicity. A possible DEM approach is to apply forces to the boundary particles of the void space to simulate the pressure inside a water-filled cavity or to apply forces related to the pore spaces between particles to simulate hydrofractures (Yoon et al., 2015). An alternative is the combination

of FEM and DEM with accountance of drag forces due to fluid flow or other combined particle-lattice model schemes (Ghani et al., 2013).

5.5   Implications for sinkhole formation at the Dead Sea

In general, the good fit of model sinkhole geometry with the observed topography of sinkholes at Ghor Al-Haditha (Section 4) confirms the suitability of the DEM approach and allows for interpretation of morphological features there. In addition, structures as found in the simulations are visible also in the field, such as sagging layers and distributed marginal fracturing in weak materials, as well as cavities, compression ridges (pop-up structures) and overhanging sides in stronger materials. For a still better fit to the low diameter results of the field (Figure 15), we would need to use a wider variety of the void space growth functions, geometries and subrosion zone depths, as expected to happen in nature. Due to computational costs, this has not been included in this study. Nonetheless, the already good agreement between the paths of depth/diameter of the existing model sinkholes as subsidence evolves and the distribution of depth/diameter values in the field (Figure 15) strongly suggests that those distributions represent growth trends of the natural sinkholes that are controlled ultimately by material properties (Figure 17).
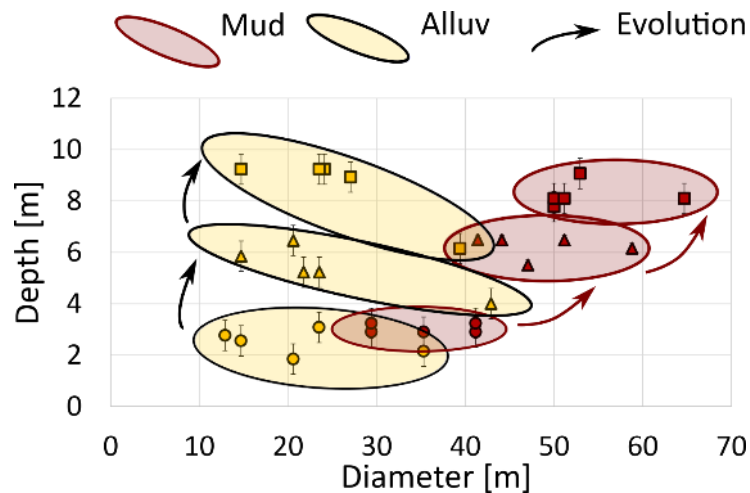
Figure 17: Simulated sinkhole depth/diameter interpretation. The simulations reveal a tendency towards deeper sinkholes in alluvium and both deeper and wider sinkholes in mud. A trend that is able to explain the observations for sinkholes at Ghor Al-Haditha.

Since material heterogeneity is the rule rather than the exception in nature, and since our simulation results fit well to seismic and photogrammetric studies in the area of Ghor Al-Haditha (Al-Halbouni et al., 2017; Polom et al., 2018) , we consider our multilayer models as favourable over uniform models for Ghor Al-Haditha. The exact values of large-scale material strength, however, due to the described material testing procedure with a constant particle packing porosity and the limitations of literature laboratory scale values under the assumption of intact rock, should be rather used carefully. Lower strength for the

materials in the field is highly probable as the observed maximum crack depth in alluvial and salt materials (4 m) is less than in the DEM simulations (up to 12 m). This is probably because in detail 'pure' sand-gravel or rock salt is rare on a large scale at the site - usually, there is plenty of muddy material interbedded. However, some general observations for the models with materials and material successions typical at the field site of Ghor Al-Haditha in Jordan can be drawn from the simulations:

1. A weak lacustrine mud layer beneath a strong cover material favours sinkhole formation. Even high strength material like the salt would collapse in such a setting.

2. A middle-deep subrosion zone (30 – 40 m) leads to collapses even for the pure alluvium models, which means that a subrosion acting only in the alluvial sediments can similarly cause sinkhole formations like those with a weak

10   interlayer. Only a higher volume removal is needed.

3. The pure salt models do not produce typical sinkholes as observed in the field zone. This fact can be related either to a lack of such a thick and strong cover material in nature or a too high strength assigned in the model. It is perhaps worth noting that at the Lisan peninsula, close to the field area at the Dead Sea, large (several meter scale) cavities and arches were observed here in Holocene Dead Sea salt (Closson et al., 2007). On the other hand, the observed salt

15   exposure at our field site contains rather thin salt layers, interleaved with mud on cm-scale, so that the bulk material strength there is expected to be lower than that simulated.

4. The possibility to record surface subsidence before actual sinkhole collapse depends on both the cover material type and the depth of the subrosion zone. A multilayer model of a middle-deep subrosion zone with a large subsurface collapse zone may produce recordable surface signatures in the order of sub cm before the onset of collapse.

Finally, the single void collapse concept explored in this paper may sufficiently explain some individual sinkhole occurrences at Ghor Haditha and elsewhere around the Dead Sea (cf. laboratory experiments by *Oz et al.*, [2016]), the coalescence, sequence evolution and sinkhole cluster structures, morphological expressions at the surface and larger sinkhole depression areas may not. For this, a more sophisticated approach of multiple void space growth, testing different geometries and a more realistic

25 subrosion process is necessary and will be addressed in a future paper.

6   Summary and conclusions

In this work, we presented a benchmarked and calibrated 2D Distinct Element Modeling approach to simulating the process of both cavity growth and sinkhole development. Our principal findings are as follows:

30 Firstly, we presented a computationally-fast DEM approach to simulating sinkhole formation by instantaneous, quasi-static, step-wise material removal in a single void space at a depth of an arbitrarily shaped geometry under gravitational loading. We

successfully benchmarked the models with analytical and BEM solutions yielding a sub-millimetre degree of agreement for surface displacements and displacement differences.

Secondly, we performed simulated compression and tension tests to determine microscopic bond strength parameters and
5   moduli calibrated by intact rock literature values and field estimates for the three materials common at the Dead Sea shoreline. The simulated rock tests yield low bulk strength (UCS ~ 0.06-0.25 MPa) for lacustrine mud, middle bulk strength (UCS ~ 0.53-0.92 MPa) for alluvial sandy-gravel sediments and high bulk strength (UCS ~ 1.23-1.54 MPa) for rock salt materials, based on Mohr-Coulomb and Hoek-Brown fits.

10   Thirdly, we simulated a cavity growth until sinkhole collapse in uniform materials. Cavity development is controlled by the interaction of the material strength and the depth of material removal. Weak materials do not support large cavities, and so subsidence is characterised by gradual sagging and suffusion type collapse into the material removal zone. Stronger materials support the development of large cavities at the material removal zone, leading to sinkhole formation by the sudden collapse of the overburden (caprock or cover collapse type sinkholes). At one end of the spectrum, near the Earth's surface, very strong
15   materials may support cavity growth until the intersection with the ground surface, giving rise to sinkholes with little or no collapse. At the other end of the spectrum, below sufficient depth and for a given material strength, the development of cavities on a significant scale is inhibited as gravitational stresses are too high.

Fourthly, we simulated a cavity growth until the sinkhole collapse in multi-layered materials. We show with the inclusion of
20   weak layers, either as cover material or as subroded bedrock material, results in sinkhole development with less volume of removed material than in the case of uniform model material. Such development is not only due to an integrated weakening of the overburden but also due to the growth of a subsurface collapse zone in the weak material that geometrically destabilises the overburden.

25   Lastly, we compare the developed morphologies from a set of models for all three materials with photogrammetric analysis from the sinkhole area of Ghor Al-Haditha in Jordan. Our approach produces physically realistic sinkhole shapes and successfully reproduces typically measured sinkhole depth to diameter ratios of 0.15 in mud-flat material, 0.37 for sinkholes in alluvium and 0.33 in salt. The field distribution appears hereby to be related to evolution stages of the sinkholes between early and late collapses. A weak (mud) interlayer and/or a deeper lying subrosion zone enhances formation of sinkholes in
30   materials typical of the Dead Sea margins.

7 Acknowledgments

We would like to thank the two reviewers and the editor for the fruitful discussion. We very gratefully acknowledge fieldwork support from Ali Sawarieh, Hussam Alrshdan and their colleagues at the Ministry of Energy and Mineral Resources of the Hashemite Kingdom of Jordan. Acknowledgements go to Emad Talafheh and Zayad Mansour from the Arab Potash Company, as well as to Michael Ezersky of the Geophysical Institute of Israel, for their support regarding geotechnical parameters. Also, we thank Arnold Verruijt for the comments regarding the analytical solution, as well as Daniel Woodell and Mehdi Nikhoo for the technical advice of the DEM and BEM modelling, respectively, and Marc Elmouttie for facilitating research stay at CSIRO (Brisbane). Special thanks go to Damien Closson and Thomas R. Walter for continuous support and material provision. We would also like to thank the reviewers and the editor for the fruitful discussion. Particular thanks go to Itasca Consulting Group for providing the license of PFC-V5.0 in the framework of the Itasca Education Partnership program and the German Academic Exchange Service (DAAD) for a short-term Doctorate research grant. Last, but not least, thanks go to the projects DESERVE and SIMULTAN and the involved colleagues for their kind support and funding opportunities.

8 References

Abelson, M., Yechieli, Y., Baer, G., Lapid, G., Behar, N., Calvo, R. and Rosensaft, M.: Natural versus human control on subsurface salt dissolution and development of thousands of sinkholes along the Dead Sea coast, J. Geophys. Res. Earth Surf., 122(6), 1262–1277, doi:10.1002/2017JF004219, 2017.

Al-Halbouni, D., Holohan, E. P., Saberi, L., Alrshdan, H., Sawarieh, A., Closson, D., Walter, T. R. and Dahm, T.: Sinkholes, subsidence and subrosion on the eastern shore of the Dead Sea as revealed by a close-range photogrammetric survey, Geomorphology, 285, 305–324, doi:10.1016/j.geomorph.2017.02.006, 2017.

Arkin, A. and Gilat, Y.: Dead Sea sinkholes – an ever-developing hazard, Environ. Geol., 39(7), 2000.

Baryakh, A. A., Stazhevskii, S. B., Timofeev, E. A. and Khan, G. N.: Strain state of a rock mass above Karst cavities, J. Min. Sci., 44(6), 531–538, 2008.

Baryakh, A. A., Rusin, E. P., Stazhevsky, S. B., Fedoseev, A. K. and Khan, G. N.: Stress-strain state of Karst areas, J. Min. Sci., 45(6), 3–10, 2009.

Bonilla-Sierra, V., Donzé, F. V, Scholtès, L. and Elmouttie, M. K.: The use of photogrammetry and 3D Discrete Element Models to better assess Rock Slope Stability., 2012.

Brady, B. H. G. and Brown, E. T.: Rock Mechanics for underground mining, 3rd ed., Springer., 2006.

Brown, E. T.: Rock characterization, testing & monitoring: ISRM suggested methods, Pergamon Press, Oxford and New York., 1981.

Byerlee, J. D.: Brittle-ductile transition in rocks, J. Geophys. Res., 73(14), 4741–4750, doi:10.1029/JB073i014p04741, 1968.

Carranza-Torres, C., Fosnacht, D. and Hudak, G. J.: Analytical and numerical study of the stability of shallow underground openings for mining and compressed air energy storage applications, edited by P. . G. . Ranjith and J. . Zhao, IC3G Int. Conf.

Geomech. Geoenergy Georesources, 2016.

Carter: Geotechnical Handbook, Pentech Press, London, Plymouth, UK., 1983.

Caudron, M., Emeriault, F., Kastner, R. and Heib, M. Al: Numerical modeling of the soil structure interaction during sinkholes., in Numerical methods in geotechnical engineering : proceedings of the 6th European conference, 6-8 september 2006, Graz, Austria, pp. 267–273., 2006.

Clément, C., Toussaint, R., Stojanova, M. and Aharonov, E.: Sinking during earthquakes: Critical acceleration criteria control drained soil liquefaction, Phys. Rev. E, 97(2), 0–19, doi:10.1103/PhysRevE.97.022905, 2018.

Closson, D. and Abou Karaki, N.: Salt karst and tectonics: sinkholes development along tension cracks between parallel strike-slip faults , Dead Sea , Jordan, Earth Surf. Process. Landforms, 34, 1408–1421, doi:10.1002/esp, 2009.

Closson, D., LaMoreaux, P. E., Abou Karaki, N. and Al-Fugha, H.: Karst system developed in salt layers of the Lisan Peninsula, Dead Sea, Jordan, Environ. Geol., 52(1), 155–172, doi:10.1007/s00254-006-0469-9, 2007.

Cundall, P. A.: A computer model for simulating progressive large scale movements in blocky rock systems, Proc. Symp. Rock Fract. (ISRM), Nancy, 1 [online] Available from: citeulike-article-id:11887443, 1971.

Cundall, P. A. and Strack, O. D. L.: A discrete numerical model for granular assemblies, Géotechnique, 29(1), 47–65 [online] Available from: citeulike-article-id:11888085, 1979.

Davis, R. O. and Selvadurai, A. P. S.: Elasticity and geomechanics, Cambridge University Press. England., 1996.

Dreybrodt, W. and Kaufmann, G.: Physics and chemistry of dissolution on subaerialy exposed soluble rocks by flowing water films, Acta Carsologica, 36(3), 357–367, 2007.

El-Naqa, A.: Application of RMR and Q geochemical classification systems along the proposed Mujib Tunnel route, Central Jordan, Bull. Eng. Geol. Environ., 60(4), 257–269, doi:10.1007/s100640100112, 2001.

Ezersky, M. and Frumkin, A.: Fault - Dissolution front relations and the Dead Sea sinkhole problem, Geomorphology, 201, 35–44, doi:10.1016/j.geomorph.2013.06.002, 2013.

Ezersky, M. and Livne, E.: Mo P 13 Geotechnical and Geophysical Properties of Soils in the Dead Sea Sinkhole Problem, in Near Surface Geoscience, Bochum, Germany., 2013.

Ezersky, M., Keydar, S., Al-Zoubi, A. and Eppelbaum, L.: Middle East Regional Cooperation Program Jordan - Sinkhole Hazard Assessment of the Dead Sea area in Israel and Jordan: Multidisciplinary study, Washington, D.C., 2013.

Ezersky, M. G., Legchenko, A., Eppelbaum, L. and Al-zoubi, A.: Overview of the geophysical studies in the Dead Sea coastal area related to evaporite karst and recent sinkhole development, Int. J. Speleol., 46(May), 277–302, doi:10.5038/1827-806X.46.2.2087, 2017.

Fakhimi, A.: Application of slightly overlapped circular particles assembly in numerical simulation of rocks with high friction angles, Eng. Geol., 74(1–2), 129–138, doi:10.1016/j.enggeo.2004.03.006, 2004.

Fazio, N. L., Perrotti, M., Lollino, P., Parise, M., Vattano, M., Madonia, G. and Di Maggio, C.: A three-dimensional back-analysis of the collapse of an underground cavity in soft rocks, Eng. Geol., 228(February), 301–311, doi:10.1016/j.enggeo.2017.08.014, 2017.

Frydman, S., Charrach, J. and Goretsky, I.: Geotechnical properties of evaporite soils of the Dead Sea area, Eng. Geol., 101(3–4), 236–244, doi:10.1016/j.enggeo.2008.06.003, 2008.

Frydman, S., Charrach, J. and Goretsky, I.: A geotechnical study of evaporitic, lacustrine sediments in the saline environment of the Dead Sea area, Eng. Geol., 181, 309–322, doi:10.1016/j.enggeo.2014.08.028, 2014.

5 Fuenkajorn, K. and Archeeploha, S.: Prediction of cavern configurations from subsidence data, Eng. Geol., 110(1–2), 21–29, doi:10.1016/j.enggeo.2009.10.003, 2010.

Ghani, I., Koehn, D., Toussaint, R. and Passchier, C. W.: Dynamic Development of Hydrofracture, Pure Appl. Geophys., 170(11), 1685–1703, doi:10.1007/s00024-012-0637-7, 2013.

Goldscheider, N. and Drew, D.: Methods in Karst Hydrogeology, edited by N. Goldscheider and D. Drew, Taylor and Francis,

10 London, UK., 2007.

Gutiérrez, F., Guerrero, J. and Lucha, P.: A genetic classification of sinkholes illustrated from evaporite paleokarst exposures in Spain, Environ. Geol., 53(5), 993–1006, doi:10.1007/s00254-007-0727-5, 2008.

Gutiérrez, F., Parise, M., De Waele, J. and Jourde, H.: A review on natural and human-induced geohazards and impacts in karst, Earth-Science Rev., 138, 61–88, doi:10.1016/j.earscirev.2014.08.002, 2014.

15 Gutiérrez, F., Fabregat, I., Roqué, C., Carbonel, D., Guerrero, J., García-Hemroso, F., Zarroca, M., Linares, R., García-Hermoso, F., Zarroca, M. and Linares, R.: Sinkholes and caves related to evaporite dissolution in a stratigraphically and structurally complex setting, Fluvia Valley, eastern Spanish Pyrenees. Geological, geomorphological and environmental implications, Geomorphology, 267(June), 76–97, doi:10.1016/j.geomorph.2016.05.018, 2016.

Hatzor, Y. H., Wainshtein, I. and Bakun Mazor, D.: Stability of shallow karstic caverns in blocky rock masses, Int. J. Rock

20 Mech. Min. Sci., 47(8), 1289–1303, doi:10.1016/j.ijrmms.2010.09.014, 2010.

Hoek, E.: Brittle Fracture of Rock, Rock Mech. Eng. Pract., 1–30, 1968.

Hoek, E.: Practical Rock Engineering, Rocscience, North Vancouver, Canada., 2007.

Hoek, E. and Brown, E. T.: Practical Estimates of Rock Mass Strength, Int. J. Rock. Min. Sci., 34(8), 1165–1186, 1997.

Hoek, E., Carranza-Torres, C. and Corkum, B.: Hoek-brown failure criterion – 2002 edition, 5th North., University of Toronto,

25 Ontario, Canada., 2002.

Holohan, E. P., Schöpfer, M. P. J. and Walsh, J. J.: Mechanical and geometric controls on the structural evolution of pit crater and caldera subsidence, J. Geophys. Res., 116(B07202), doi:10.1029/2010JB008032, 2011.

Holohan, E. P., Schöpfer, M. P. J. and Walsh, J. J.: Stress evolution during caldera collapse, Earth Planet. Sci. Lett., 421, 139–151, doi:10.1016/j.epsl.2015.03.003, 2015.

30 Holohan, E. P., Sudhaus, H., Walter, T. R., Schöpfer, M. P. J. and Walsh, J. J.: Effects of Host-rock Fracturing on Elastic-deformation Source Models of Volcano Deflation, Sci. Rep., 7(1), 10970, doi:10.1038/s41598-017-10009-6, 2017.

Itasca Cooperation Group, I.: PFC 5.0 Manual, 2014.

Ivars, D. M., Pierce, M. E., Darcel, C., Reyes-Montes, J., Potyondy, D. O., Paul Young, R. and Cundall, P. A.: The synthetic rock mass approach for jointed rock mass modelling, Int. J. Rock Mech. Min. Sci., 48(2), 219–244,

doi:10.1016/j.ijrmms.2010.11.014, 2011.

Jaeger, J. C., Cook, N. G. W. and Zimmerman, R.: Fundamentals of rock mechanics, 4th ed., Wiley - Blackwell., 2007.

Jing, L. and Stephansson, O.: Fundamentals of Discrete Element Methods for Rock Engineering I, Elsevier., 2007.

Kaufmann, G. and Romanov, D.: Structure and evolution of collapse sinkholes : Combined interpretation from physico-chemical modelling and geophysical field work, J. Hydrol., 17, 2958, doi:10.1016/j.jhydrol.2016.06.050, 2016.

Khanal, M. and Schubert, W.: DEM simulation of diametrical compression test on particle compounds, Granul. Matter, 7, 83–90, doi:10.1007/s10035-005-0200-7, 2005.

Khoury, H. N.: Clays and clay minerals in Jordan, Amman, Jordan., 2002.

Kirsch, E. G.: Die Theorie der Elastizität und die Bedürfnisse der Festigkeitslehre., Zeitschrift des Vereines Dtsch. Ingenieure, 42, 797–807, 1898.

Koolen, A. J. and Vaandrager, P.: Relationships between soil mechanical properties, J. Agric. Eng. Res., 29(4), 313–319, doi:10.1016/0021-8634(84)90086-6, 1984.

Manger, E. G.: Porosity and Bulk Density of Sedimentary Rocks, edited by S. Udall and T. Nolan, US Government Printing Office, Washington, D.C., 1963.

Mercerat, E. D.: Évaluation de l'endommagement dans le recouvrement d'une cavité saline par une approche numérique couplée continue-discrète, in XXVèmes Rencontres Universitaires de Genie Civil, Nancy, France., 2007.

Mindlin, R. D.: Stress distribution around a tunnel, Trans. Am. Soc. Civ. Eng., (2082), 1117–1153, 1940.

Muskhelishvili, N. I.: Singular Integral Equations: Boundary Problems of Functions Theory and Their Application to Mathematical Physics, P. Noordhoff., 1953.

Muskhelishvili, N. I.: Some basic problems of the mathematical theory of elasticity, Springer Science & Business Media., 2013.

Nikkhoo, M. and Walter, T. R.: Triangular dislocation: an analytical, artefact-free solution, Geophys. J. Int., 201(2), 1119–1141, doi:10.1093/gji/ggv035, 2015.

Oz, I., Eyal, S., Yoseph, Y., Ittai, G., Elad, L. and Haim, G.: Salt dissolution and sinkhole formation: Results of laboratory experiments, J. Geophys. Res. Earth Surf., 1–17, doi:10.1002/2016JF003902.Received, 2016.

Parise, M. and Gunn, J.: Natural and anthropogenic hazards in karst areas: recognition, analysis and mitigation, Geological Society of London., 2007.

Parise, M. and Lollino, P.: A preliminary analysis of failure mechanisms in karst and man-made underground caves in Southern Italy, Geomorphology, 134(1–2), 132–143, doi:10.1016/j.geomorph.2011.06.008, 2011.

Parise, M., Gabrovsek, F., Kaufmann, G. and Ravbar, N.: Recent advances in karst research: from theory to fieldwork and applications, Geol. Soc. London, Spec. Publ., SP466.26, doi:10.1144/SP466.26, 2018.

Polom, U., Alrshdan, H., Al-Halbouni, D., Sawarieh, A., Dahm, T. and Krawczyk, C.: Improved Dead Sea sinkhole site characterization at Ghor Al Haditha, Jordan, based on repeated shear wave reflection seismic profiling, in EGU General Assembly, Vienna, Austria., 2016.

Polom, U., Alrshdan, H., Al-Halbouni, D., Dahm, T., Sawarieh, A., Atallah, M. Y. and Krawczyk, C. M.: Shear wave reflection seismics yields subsurface dissolution and subrosion patterns: application to the Ghor Al-Haditha sinkhole site, Dead Sea, Jordan, Solid Earth, 9(Environmental changes and hazards in the Dead Sea region), 1079–1098, doi:https://doi.org/10.5194/se-9-1079-2018, 2018.

5   Poppe, S., Holohan, E. P., Pauwels, E., Cnudde, V. and Kervyn, M.: Sinkholes, pit craters, and small calderas: Analog models of depletioninduced collapse analyzed by computed X-ray microtomography, Bull. Geol. Soc. Am., 127(1–2), 281–296, doi:10.1130/B30989.1, 2015.

Potyondy, D.: Material-Modeling Support in PFC, Minneapolis, Minnesota, USA., 2014a.

Potyondy, D. O.: The bonded-particle model as a tool for rock mechanics research and application: current trends and future

10   directions, Geosystem Eng., 17(6), 342–369, 2014b.

Potyondy, D. O. and Cundall, P. a. A.: A bonded-particle model for rock, Int. J. Rock Mech. Min. Sci., 41(8), 1329–1364, doi:10.1016/j.ijrmms.2004.09.011, 2004.

Rawal, K., Wang, Z.-M. and Hu, L.-B.: Exploring the Geomechanics of Sinkholes: A Numerical Study of Sinkhole Subsidence and Collapse, Geo-China 2016, (December), 1–8, doi:10.1061/9780784480007.001, 2016.

15   Sainsbury, B.: A model for cave propagation and subsidence assessment in jointed rock masses, University of South Wales., 2012.

Salmi, E. F., Nazem, M. and Giacomini, A.: A Numerical Investigation of Sinkhole Subsidence Development over Shallow Excavations in Tectonised Weak Rocks: The Dolaei Tunnel's Excavation Case, Geotech. Geol. Eng., 35(4), 1685–1716, doi:10.1007/s10706-017-0202-3, 2017.

20   Sawarieh, A., Al Adas, A., Al Bashish, A. and Al Seba'i, E.: Sinkholes Phenomena At Ghor Al Haditha Area - Internal Report No. 12, Amman, Jordan., 2000.

Schöpfer, M. P. J., Childs, C. and Walsh, J. J.: Two-dimensional distinct element modeling of the structure and growth of normal faults in multilayer sequences: 1. Model calibration, boundary conditions, and selected results, J. Geophys. Res., 112(B10), B10401, doi:10.1029/2006JB004902, 2007.

25   Schöpfer, M. P. J., Abe, S., Childs, C. and Walsh, J. J.: The impact of porosity and crack density on the elasticity, strength and friction of cohesive granular materials: Insights from DEM modelling, Int. J. Rock Mech. Min. Sci., 46(2), 250–261, doi:10.1016/j.ijrmms.2008.03.009, 2009.

Schöpfer, M. P. J., Childs, C. and Manzocchi, T.: Three-dimensional failure envelopes and the brittle-ductile transition, J. Geophys. Res. Solid Earth, 118(4), 1378–1392, doi:10.1002/jgrb.50081, 2013.

30   Schöpfer, M. P. J., Childs, C., Manzocchi, T. and Walsh, J. J.: Three-dimensional Distinct Element Method modelling of the growth of normal faults in layered sequences, Geol. Soc. London, Spec. Publ., 439, SP439.17, doi:10.1144/SP439.17, 2016.

Schöpfer, M. P. J., Childs, C., Manzocchi, T., Walsh, J. J., Nicol, A. and Grasemann, B.: The emergence of asymmetric normal fault systems under symmetric boundary conditions, J. Struct. Geol., 104(May 2016), 159–171, doi:10.1016/j.jsg.2017.10.006, 2017.

Schultz, R. A.: Relative scale and the strength and deformability of rock masses, J. Struct. Geol., 18(9), 1139–1149, doi:10.1016/0191-8141(96)00045-4, 1996.

Shalev, E. and Lyakhovsky, V.: Viscoelastic damage modeling of sinkhole formation, J. Struct. Geol., 42, 163–170, doi:10.1016/j.jsg.2012.05.010, 2012.

5 Taqieddin, S. a., Abderahman, N. S. and Atallah, M.: Sinkhole hazards along the eastern Dead Sea shoreline area, Jordan: a geological and geotechnical consideration, Environ. Geol., 39(11), 1237–1253, doi:10.1007/s002549900095, 2000.

Terzaghi, K.: Rock Defects and loads on Tunnel Supports, Harvard Univ. PP - Massachusetts., 1946.

Tharp, T. M.: Mechanics of upward propagation of cover-collapse sinkholes, Eng. Geol., 52(1–2), 23–33, doi:10.1016/S0013-7952(98)00051-9, 1999.

10 Thompson, N., Bennett, M. R. and Petford, N.: Development of characteristic volcanic debris avalanche deposit structures: New insight from distinct element simulations, J. Volcanol. Geotherm. Res., 192(3), 191–200, doi:https://doi.org/10.1016/j.jvolgeores.2010.02.021, 2010.

Timoshenko, S. P. and Goodier, J. N.: Theory of Elasticity, Internatio., Kogakusha Company Ltd., Tokyo., 1973.

Verlet, L.: Computer "Experiments" on Classical Fluids. I. Thermodynamical Properties of Lennard-Jones Molecules, Phys.
15 Rev., 159(1), 1967.

Verruijt, A. and Booker, J. R.: Complex variable analysis of Mindlin's tunnel problem, Dev. Theor. Geomech., 1–20, 2000.

Verruijt, A. and Booker, J. R.: Complex Variable Solution of Mindlin's Problem of an Excavated Tunnel (background material of the publication by Verruijt & Booker (2000)), Dev. Theor. Geomech., 2009.

Wadas, S. H., Polom, U. and Krawczyk, C.: High-resolution shear wave reflection seismics as a tool to image near-surface
20 subrosion structures - a case study in Bad Frankenhausen, Germany, Solid Earth, 7, 1491–1508, doi:10.5194/se-7-1491-2016, 2016.

Waltham, T., Bell, F. and Culshaw, M. G.: Sinkholes and subsidence: Karst and Cavernous Rocks in Engineering and Construction, Springer, Berlin, Heidelberg., 2005.

Watson, R. A., Holohan, E. P., Al-Halbouni, D., Saberi, L., Sawarieh, A., Closson, D., Alrshdan, H., Abou Karaki, N., Siebert,
25 C., Walter, T. R., Dahm, T., Karaki, N. A., Siebert, C., Walter, T. R. and Dahm, T.: Sinkholes, stream channels and base-level fall: a 50-year record of spatio-temporal development on the eastern shore of the Dead Sea, Solid Earth Discuss., doi:https://doi.org/10.5194/se-2018-105, 2018.

Yechieli, Y., Abelson, M., Bein, A., Crouvi, O. and Shtivelman, V.: Sinkhole "swarms" along the Dead Sea coast: Reflection of disturbance of lake and adjacent groundwater systems, Geol. Soc. Am. Bull., 118(9–10), 1075–1087, doi:10.1130/B25880.1,
30 2006.

Yizhaq, H., Raz, E., Ashkenazy, Y., Cohen, C., Raz, E. and Ashkenazy, Y.: Scale-free distribution of Dead Sea sinkholes : Observations and modeling, Geophys. Res. Lett., 44(00940v1), 1–9, doi:10.1002/2017GL073655.Received, 2017.

Yoon, J. S., Zimmermann, G. and Zang, A.: Numerical Investigation on Stress Shadowing in Fluid Injection-Induced Fracture Propagation in Naturally Fractured Geothermal Reservoirs, Rock Mech. Rock Eng., 48(4), 1439–1454, doi:10.1007/s00603-

014-0695-5, 2015.

Zeev, S. Ben, Goren, L., Parez, S., Toussaint, R., Clement, C. and Aharonov, E.: The Combined Effect of Buoyancy and Excess Pore Pressure in Facilitating Soil Liquefaction, in Poromechanics VI, pp. 107–116., 2017.

Zhu, T.: Some useful numbers on the engineering properties of materials (geologic and otherwise), [online] Available from:

5   https://www.jsg.utexas.edu/tyzhu/files/Some-Useful-Numbers.pdf (Accessed 23 February 2018), 2010.

Appendix A   The Distinct Element Method and its use for simulating geo-materials

The Distinct Element Method (DEM) is a specific scheme of undeformable particles and deformable contacts developed by

10   (Cundall, 1971). In the software Particle Flow Code in Two Dimensions (PFC2D-V5.035), the DEM is used to implement Newton-Euler equations of motion and rotation on disk-shaped particles (Itasca Cooperation Group, 2014; Potyondy, 2014a; Potyondy and Cundall, 2004) (Figure 18A). In PFC, the resolution scheme is an explicit second-order Velocity Verlet algorithm (Verlet, 1967). The particles are assigned a mass and a radius, are initially unbonded, and are free to move and rotate depending on external forces. Particles interact only at contact points between particles and wall facets, where the mechanical

15   interaction is treated in terms of a frictional contact with a set of linear elastic springs that are assigned normal and shear stiffness (Figure 18B). The 'rigidity' of the particles is defined by setting the elastic Young's constant in accordance to the spring stiffness. An additional bonding of the elements can be performed, whereby many different bond types can be specified. Here we use the parallel-bond model [*Potyondy and Cundall*, 2004], which is defined in terms of a set of linear elastic springs in parallel to the linear contact bond. The parallel bonds allow for tensile forces and bending moments between the bonded

20   particles, and they break once their strength is exceeded. Here we set the bonds to have the same material constants (microproperties) as the particles, like stiffness, elastic modulus, but since bond strength is defined similar to a Mohr-Coulomb failure criterion, the bonds are also assigned a cohesion, tensile strength and friction angle (Figure 18C).
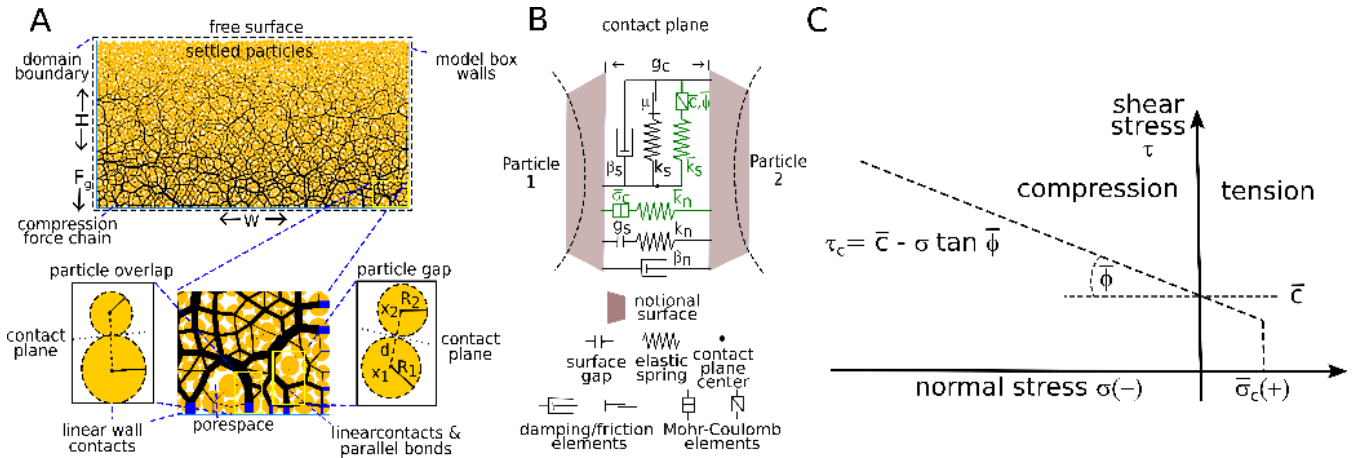
Figure 18: Schematic description of 2D-DEM modelling with PFC2D-V5. (A) inter-particle and particle-wall force chains developed after gravity settling of an assembly of balls in a box of dimension H x W. The close-ups below show the pore space, contact planes and nomenclature. Particles, although undeformable, are allowed to overlap slightly or have a small gap g_c. In both cases, linear contacts and optional parallel bonds are active. These bonds act additionally to the linear contacts. (B) close-up of the notional and contact planes with all elements necessary for the physical definition of the contact and bond interactions. (C) failure criterion for parallel bonds. Compression in this study is considered as negative.

A.1 Mathematical details of the DEM method implemented in the PFC software

The Newton-Euler equations are solved in a finite difference explicit time-stepping algorithm involving dynamic relaxation (Cundall, 1971; Jing and Stephansson, 2007). During the procedure, Newton's second law and the force-displacement law is solved for each of the particles and its contacts (Potyondy and Cundall, 2004). For a 2D system of coupled rigid elements, the differential equations solved by the explicit time-marching relaxation scheme for a particle of mass m are (Jing and Stephansson, 2007):

$$m\ddot{u}_x^t + \alpha m\dot{u}_x^t = F_x, \ m\ddot{u}_y^t + \alpha m\dot{u}_y^t = F_y, \ I\ddot{\theta}^t + \alpha I\dot{\theta}^t = M \qquad (2)$$

with F as force, u as displacement, $\dot{u}$ as velocity, $\ddot{u}$ as acceleration, α as damping, M as moment of force, I as inertia, θ as Euler rotation angle, $\dot{\theta}$ as Euler rotation velocity and $\ddot{\theta}$ as Euler rotation acceleration at a certain time t.

It is assumed that (1) velocities and accelerations within one timestep are constant and (2) that the step chosen is small enough that disturbances, which occur due to external or body forces, particle or boundary wall movement, propagate only to the neighbours of the particles. The resulting velocity and acceleration components for both the translational and rotational motion of one particle are determined via a finite difference scheme successively for each timestep t (Jing and Stephansson, 2007):

$$\ddot{u}_i^t = \frac{1}{(\Delta t)^2}\left(u_i^{t+1} - 2u_i^t + u_i^{t-1}\right), \ \dot{u}_i^t = \frac{1}{2\Delta t}\left(u_i^{t+1} - u_i^{t-1}\right) \qquad (3)$$

with i as x or y and the equations for $\dot{\theta}$ and $\ddot{\theta}$ accordingly. The displacement calculation is generally one timestep ahead of velocities/accelerations calculation, and constitutive laws of arbitrary complexity (Jing and Stephansson, 2007) can be added between the contacts without numerical instability. The kinematic critical timestep $\Delta t_{crit} = \min(\sqrt{\frac{m_i}{k_i}})$ is determined for an infinite multiple set of masses m_i and springs with stiffnesses k_i to allow for the above contraints and solution of the equations.

5   The equilibrium is defined by a convergence criterion, where the ratio between the "out-of-balance" forces to the overall forces is below a defined threshold (Solve Ratio, SR), usually 1^{-5} or lower. This "solving" can be performed for the mean (SR$_{mean}$) or maximum (SR$_{max}$) forces that appear in the model. A problem can occur when absolute normal force calculation during material gravity settling is used: Interlocked forces due to the particle overlap may not be released during further simulation. This issue has been overcome by introducing an incremental normal force calculation (Fakhimi, 2004) which is implemented in PFC2D-

10   v5 (Itasca Cooperation Group, 2014; Potyondy, 2014b).

A.2 Creating a gravitationally-loaded synthetic rock mass in the DEM

Creation of a bonded particle assembly in this study followed that of *Holohan et al.*, [2011] and involved the following chain

15   of steps:

1. **Creation of an unbonded particle assembly** of defined particle sizes, porosity and geometrical distribution. A uniform distribution of particles between a defined minimum and maximum radius are placed randomly in the model box of size H x W The unbonded material is limited by three walls with low friction (0.01) elastic interaction. The radii distribution in this study is chosen to be equal between the minimum and maximum

20   assigned radius (Table 7) according to the defined porosity.

2. **Assignment of material domains:** The mechanical properties are distributed in the assembly according to the desired model setup, e.g. layering. The linear contact model is installed between each two entities at a distance smaller or equal to the surface gap.

3. **Gravity settling:** Gravity acts as the main body force. A settling criterion is applied, i.e. the material is considered

25   as settled when a certain threshold, here $SR_{mean} = 1^{-6}$, of the velocity and displacement change of the particles between two timesteps is reached. The material is settled under low friction until the defined solve ratio.

4. **Particle bonding:** The created assembly contains, as real rock, interlocked forces. Now the particle bonding is applied according to a chosen bond type (parallel) and the model is cycled into equilibrium. Linear contact friction is set to the defined value.

At each step, the material assembly is cycled until a static equilibrium is reached. The behaviour of a DEM model depends strongly on the material packing assembly (Schöpfer et al., 2009), and so a spectrum of solutions is usually obtained by performing multiple realizations for different assemblies. The above chain is thus repeated to produce many random particle

assemblies that may be used to obtain a statistical mean of packing-dependent model outcomes. In this study, the procedure was repeated generally for 5-10 random assemblies of the particles.

Appendix B   Details on model covergence tests, benchmarking, material calibration and the final sinkhole model implementation

The following section gives an overview over the performed DEM model convergence, void space installation and benchmarking tests that were performed to determine the optimal sinkhole formation modelling setup. Table 7 summarizes the main DEM model parameters used for the tests.

Table 7: Dimensions of the model and contact and particle properties used in development and testing of DEM cavity formation models.

Geometric parameter or Micro-parameter	Symbol	Unit	Value range (common)
Model height	H	[m]	100-500 (400)
Model width	W	[m]	100-500 (400)
Material porosity	n		0.2
Minimum particle radius	R_{min}	[m]	4.98-0.17 (0.24)
Mean particle radius	$\bar{R}$	[m]	6.65-0.23 (0.32)
Particle radius factor	R_f		1.66
Particle density	ρ	[kg/m^3]	2500
Solve ratio unbalanced/balanced forces	SR		1^{-6}
Cavity centre depth	h	[m]	35
Cavity radius	r	[m]	5
Boundary walls Young's modulus	E_W	[GPa]	-5
Parallel bond Young's modulus	E_{Pb}	[GPa]	-5
Parallel bond tensile strength	$\bar{\sigma}_c$	[MPa]	1000
Parallel bond cohesion	$\bar{c}$	[MPa]	1000
Parallel bond friction angle	ϕ	[°]	30
Parallel bond ratio normal/shear stiffness	$\bar{k}_n/\bar{k}_s$		2.5
Linear contact Young's modulus	E	[GPa]	-5
Linear contact friction coefficient	μ		0.01-0.5 (0.5)
Linear contact normal/shear stiffness ratio	k_n/k_s		2.5
Linear contact normal/shear damping	β_n/β_s		0.7/0.0
Surface gap	gs	[m]	$2.1^{-2} * R_{min}$ (= 5.04^{-3})
Gravitational acceleration	G	[m/s^2]	9.81

B.1 Comparison of cavity generation methods

Several methods have been tested in order to determine the optimal void installation procedure for reasonable simulation time and realistic surface displacement curves. These are: Instantaneous material removal by particle deletion (M1), incremental material removal by particle deletion (M2), whole cavity particle radii reduction (M3) and incremental particle radii reduction (M4). The radius (r = 5 m) and centre depth (h = 35 m) of the circular material removal zone was chosen to match the expected sizes of cavities at the area of application. In M1, particles inside the cavity are instantaneously removed, while M2 allows for 15 steps of incremental particle deletion. For the other two methods parallel-bonds are first removed and then we use particle radii reduction in 50 steps to 7.7 % of the original size, each step meaning 5 % reduction. The difference between both is again a complete (M3) vs. incremental (M4) approach. In all methods, the assembly is cycled to $SR_{max}=1e\text{-}6$.

M3 and M4 show similar results for the horizontal displacement U_x but a slightly lower vertical displacement U_y compared with M1 & M2 (Figure 19). A crucial finding is that M3 & M4 reveal a by 1-2 orders of magnitude longer calculation time. As a result of this test, we consider methods M1 and M2 as generally suitable to simulate a realistic material removal under acceptable calculation time. For the following model verification tests, we rely on method M1 as the simplest option to implement a cavity and M2 will serve for the final sinkhole models.
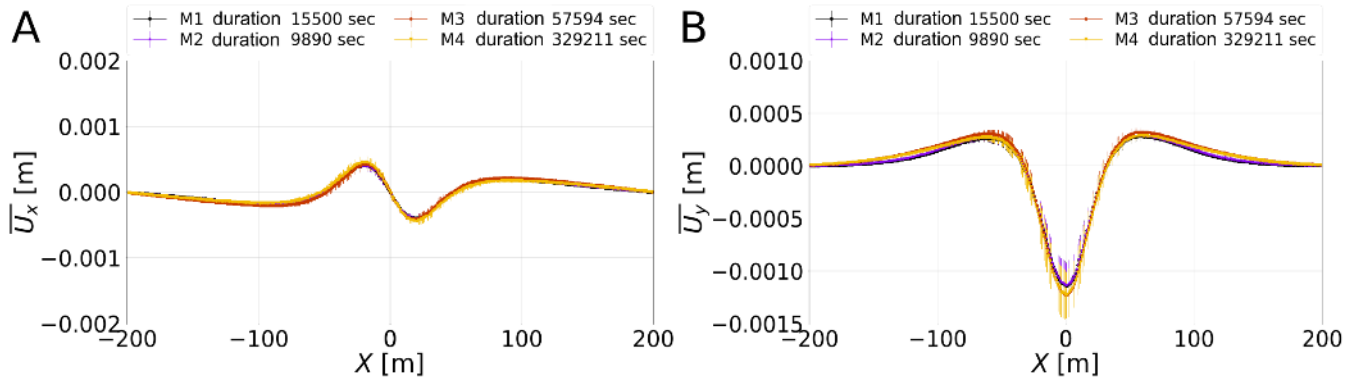
Figure 19: Displacement plots for different void installation methods. (A) Horizontal and (B) vertical model setup with size 400 x 400 m using a coarse particle distribution (mean radius 0.74 m). Indication of needed simulation time is given in the legend. M1-M4 refers to the installation method described in the text.

B.2 Convergence tests on model dimensions and resolution

We performed model resolution tests to determine the optimal size for the mechanical problem of a shallow cavity in a bonded rock assembly. The cavity is installed by instantaneous (quasi-static) particle removal (M1 as shown in Figure 4A). We varied

the width W and height H of the model box from 100-800 m while keeping the particle radii constant at 0.74 m for a cavity installation in 35 m depth with a radius of 5 m and track the horizontal and vertical surface displacement.

In Figure 20 we see the horizontal and vertical displacement curves for all model dimensions. Boundary effects in such a setting close to the free surface make the judgement of the optimal size demanding, but the expected behaviour for the vertical displacement is a subsidence roughly 9/10 and an uplift roughly 1/10 of the total vertical displacement (cf. model benchmarking in Section 2.2).
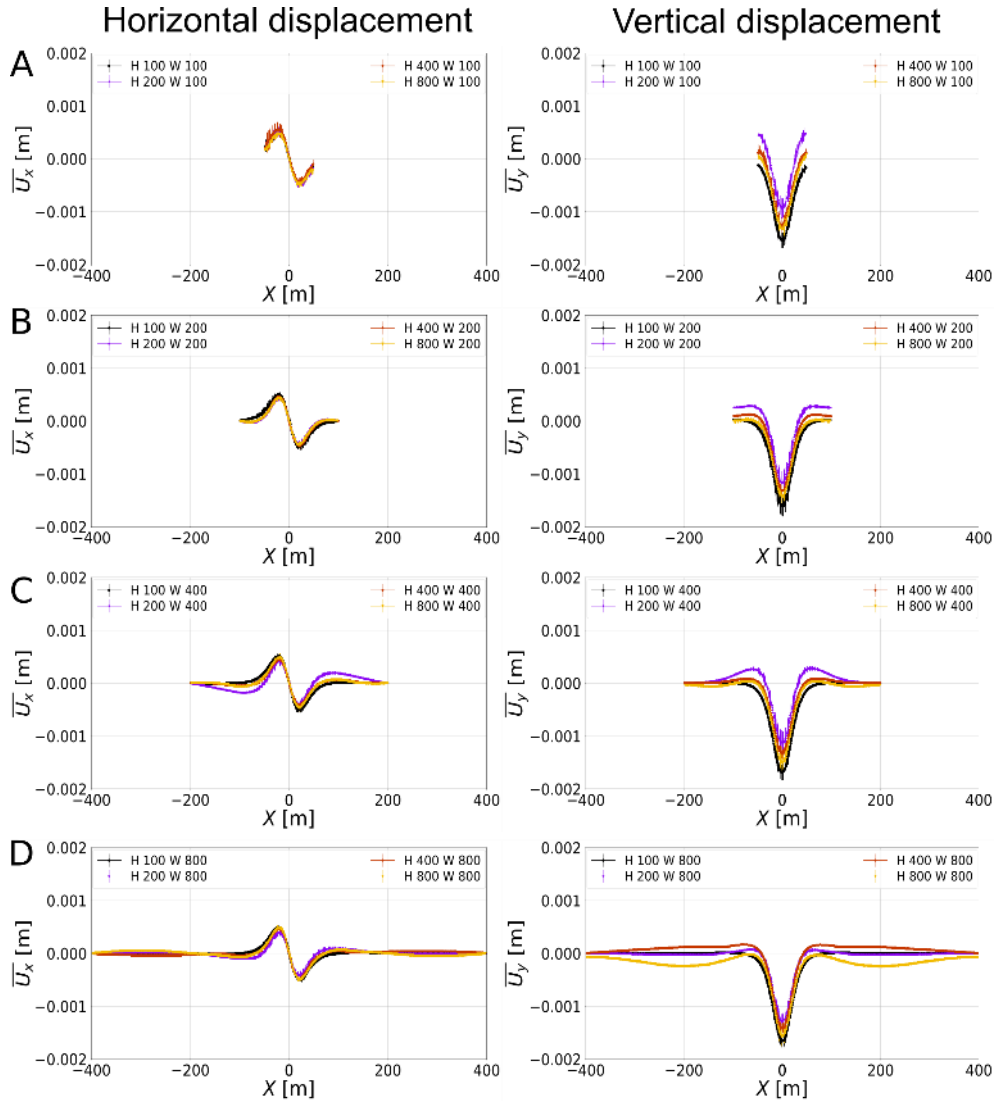
Figure 20: Convergence test results for model assembly dimensions: Cavity of radius = 5 m and depth = 35 m created in each case by method M1. Mean particle radius is 0.74 m. Left and right columns show horizontal and vertical displacement profiles, respectively. Each plot shows results for varying model height (H) from 100-800 m for a given width (W). In parts (A) W = 100 m;

(B) W = 200 m; (C) W = 400 m; (D) W = 800 m. A convergence is observed for larger model dimensions and a minimum height of 400 m is favoured. Symmetric boundaries (400 x 400 m) give the most stable results.

We observe the most stable results for symmetric model dimensions and define the optimal model size to height (H) x width (W) = 400 x 400 m to account for later possible growth of such a void space. In relation to the cavity size, this means the optimal model is 40 x cavity diameter. In another expression, the optimal model dimension/cavity depth ratio is 10, a typical value in engineering problems (cf. B.3). In detail, asymmetric or small model sizes lead to instable results with tails not reaching the expected zero line.

The influence of the particle radii on the displacement curves is shown in Figure 21 for the above determined favourable model dimensions. A convergence is observed for particles with mean radius around 0.32 m. Model dimensions of H x W = 400 x 400 m with a mean particle radius of $\bar{R} = 0.32$ m are thus the optimum parameters to account for converging results, model boundary effects and minimizing simulation times.
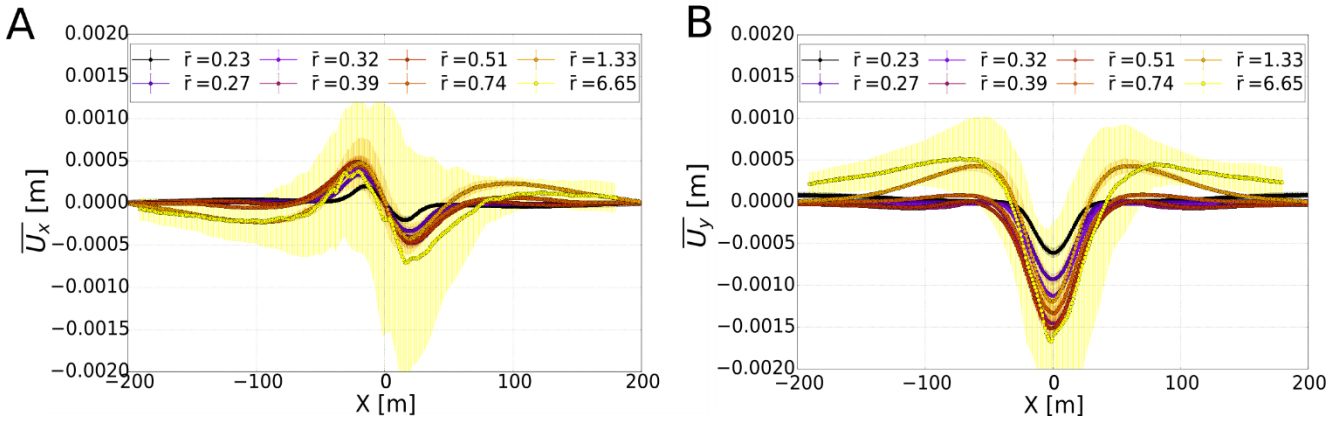
Figure 21: Results of convergence tests of for influence of particle size: Horizontal (A) and vertical displacement (B) profiles for method M1 with in a 400 x 400 m sized box. We observe a convergence of the displacement curves for mean radii around 0.32 m but for decreasing particle sizes a further diminishing of the amplitudes.

B.3 Detailed of continuum-based solutions for displacements around a gravitationally-loaded cavity in 2D

The first analytical solution used, the Kirsch solution, a classical solution for simple excavation shapes, does not include the free-surface effect and the mathematical details are depicted e.g. in (Brady and Brown, 2006). The radial and tangential displacements at a point $\boldsymbol{a} = \boldsymbol{a}(a, \theta)$ at the surface for an average vertical stress P, the horizontal stress K*P and the shear modulus G are:

$$u_r(\boldsymbol{a}, \theta) = \frac{Pr^2}{4G|a|} \left((1 + K) - (1 - K) * (4 * (1 - v) - \frac{r^2}{|a|}) \cos 2\theta \right) \tag{4}$$

$$u_t(a, \theta) = \frac{Pr^2}{4G|a|} \left((1 - K) * (2 * (1 - 2 * v) + \frac{r^2}{|a|}\right) \sin 2\Theta \qquad (5)$$

With translation into Cartesian coordinates this yields the surface displacements:

$$u_{xx}(y = 0) = u_r \cos 2\theta - u_t \sin 2\theta \qquad (6)$$

$$u_{yy}(y = 0) = u_r \sin 2\theta + u_t \cos 2\theta \qquad (7)$$

The second analytical solution used is from *Verruijt and Booker*, [2009], and includes the free-surface effect and is based on the analytical solution of stresses from *Mindlin*, 1940. *Verruijt and Booker*, [2009], added the displacement calculation to the original 2D Mindlin solution. It is determined via the complex variable method (Muskhelishvili, 1953) and consists of three partial solutions. The second and third partial solutions are relevant for displacement calculation. The second is based on Melan's solution for a concentrated vertical force in a semi-infinite medium and the third involves a balance of the stresses at the cavity boundary. The reader is referred to *Verruijt and Booker*, [2000, 2009], for mathematical details.

The equation for normal displacements as derived by the second solution for an elastic half space (x, y) under the action of normal line surface load *P* (Melan's solution) is (Davis and Selvadurai, 1996; Jaeger et al., 2007):

$$u_{yy}(x, y) = \frac{(1-v)P}{G\pi} [\![\ln(x + a)]\!]_{x=0}^{x=\infty} \qquad (8)$$

with G the Lamé parameter (shear modulus), v the Poisson-ratio and a the distance to the point of interest.

As well-know from linear elastic material theory (Muskhelishvili, 2013; Timoshenko and Goodier, 1973) the integration of the stress formulae is such a setting of a loaded material (Flamant's problem), which is similar to material removal in the underground, leads to the logarithmic term in the equation above. This leads to infinite vertical displacements along the x-surface and a singularity at the centre point $(x, y = 0)$.

As a workaround for calculation of finite displacements around the cavity, *Verruijt and Booker*, [2009], defined a value *d* where displacements are set to zero, $u_{yy}(y = d, x = 0) = 0$, a so-called fixed point at depth. This constant *d* can be arbitrarily defined, in engineering it is usually set to ten times the depth of the cavity (d $= 10 * $ h).

Thus, displacements are considered as not physically realistic in the far-field of a load (or cavity), but relative displacement differences are (cf. *Davis and Selvadurai*, [1996] and *Verruijt and Booker*, [2009]). For the above stated problem the relative

vertical displacements $\Delta u_{yy} = u_{yy}(x_1) - u_{yy}(x_2)$ between two points x_1 and x_2 at the surface is (Davis and Selvadurai, 1996):

$$\Delta u_{yy} = \frac{(1-v)P}{G\pi} \ln\frac{x_1}{x_2}$$

(9)

Figure 22 highlights the effect of a variation in Young's modulus and the fixed point depth on the fit between modelled vertical displacements and the analytical Mindlin solution described above. A general finding is that E determines the amplitude of the curve and one can gain even better fits of the DEM results when using a higher elasticity module than determined by the simulated rock tests. Furthermore, setting the d/h value to a more realistic value such as 11.43 which

10 corresponds to a cavity central depth of 35 m and a model height of 400 m, shifts the entire vertical displacement curve. The displacement difference is not affected by this integration constant. Hence, when considering the final "best-fit" solution with a low d/h = 4 and high elastic modulus E > 10 GPa, the difficulty in cancelling out the integration constant of the analytical displacement solution leaves a still poor fit of the DEM results in the far-field but a reasonable fit in the near-field of the installed cavity. We use this approach to determine the near-field at the surface as approximately $-8r \leq x \leq 8r$ with

15 r the radius of the cavity. In our case this means that the surface near-field limits are ± 40 m from the centre of the depression.
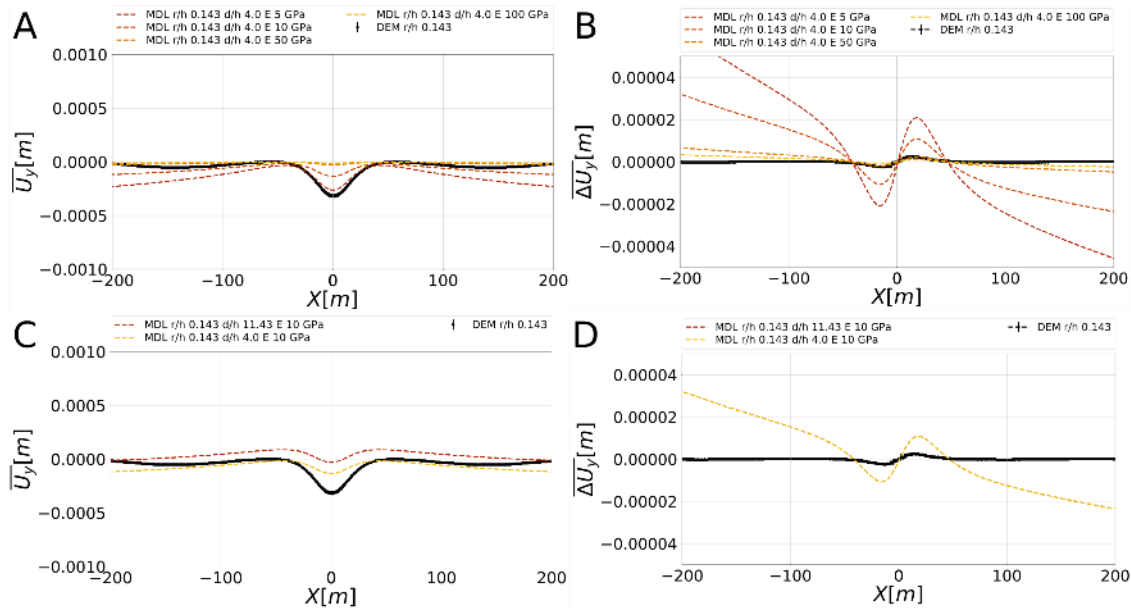
Figure 22: The effect of Young's modulus E and fixed depth point d/h on the vertical displacement (left column) and displacement difference (right column) of the Mindlin (MDL) analytical solution as calculated by *Verruijt and Booker*, **[2009]. A and B show the**

20 **scaling effect of the elastic modulus which affects both** U_y **and** ΔU_y. **C and D show the effect of d/h for** $E = 10\ GPa$ **which shifts the** U_y **curve but has no effect on** ΔU_y.

B.4 Details on Mohr-Coulomb and Hoek-Brown rock test analysis

The bulk behaviour of particle assemblies emerges from the interaction of the particle according to the mechanical rules imposed at the contact and bond scale. Therefore, and unlike for continuum-based approaches, the bulk behaviour in DEM models must be calibrated by simulated rock or soil mechanics tests (Potyondy and Cundall, 2004) . Here biaxial compression and tension tests are used to determine the bulk elastic properties of the medium, i.e. the Poisson-ratio ν and Young's elastic modulus E. By fitting of the peak stress data upon failure in such tests to e.g. Mohr-Coulomb or Hoek-Brown failure envelopes, one can also determine bulk strength properties (tensile strength T, unconfined compressive strength UCS, coefficient of internal friction ϕ).
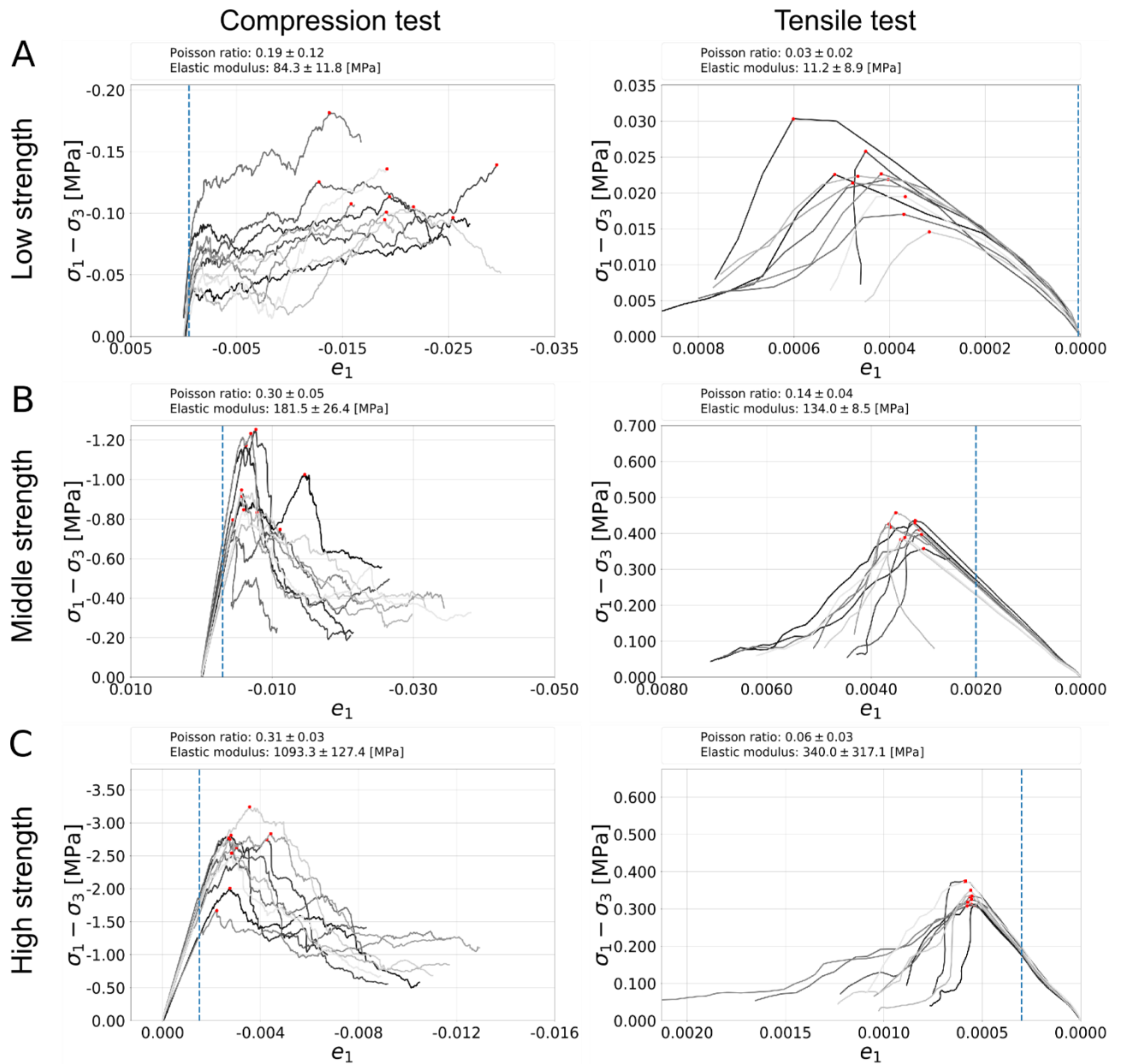
Figure 23: Differential stress vs. vertical strain for CC and DT tests for a confining pressure of 0.1 MPa. (A) Lacustrine mud; (B) Alluvium sediments; (C) Holocene salt rock. Dashed line indicates elastic limit which was used to determine elastic parameters displayed above the graphs. Red dots mark the peak stresses.

5   A typical stress vs. strain curve contains three parts: (1) a non-linear or linear elastic behaviour, (2) a non-linear yielding behaviour as cracks appear in the material and (3) a non-linear post-peak behaviour after material failure. The peak of the stress-strain curve defines the maximum and minimum principal stresses (σ_1,σ_3) at failure. For the compression test the axial stress is the maximum compressive stress σ_1 (most negative value in the convention used here) and the transversal stress is the

minimum compressive stress σ_3 (least negative). For the tension test it is vice versa, the transversal stress is the maximum tensile stress σ_1 (most positive) and the axial stress is the minimum tensile stress σ_3 (least positive).

The mean peak stresses can be determined for each confining pressure and plotted against each other. In a linear (Mohr-Coulomb) fit of $\sigma_1(\sigma_3)$, the UCS is determined by the intercept at $\sigma_3 = 0$, the unconfined tensile strength (T) by the intercept at $\sigma_1 = 0$. The slope $q = tan^2\beta$ can be used to fit the Mohr-failure envelope as shown in Figure 7:

$$\sigma_1 = C + \sigma_3\, tan^2\beta \qquad\qquad (\ 10\ )$$

with $C = UCS = 2c_0 \tan\beta$ and $\beta = 45° + \phi/2$. For a Hoek-Brown fit in a $\sigma_1(\sigma_3)$ plot a function of the following form is used:

$$\sigma_1 = \sigma_3 + \sqrt{m\sigma_0\sigma_3 + s{\sigma_0}^2} \qquad\qquad (\ 11\ )$$

with m and s as the empirical rock parameters. For the assumption of intact rock, s = 1, $\sigma_0 = C$, the UCS and $T \sim \frac{C}{m}$. The fit parameters m and C hence are used to derive the strength properties of the tested materials. Figure 23 provides exemplary stress vs. strain plots at a confining pressure of -0.1 MPa for all tested materials.

B.5 Technical details of implementation of cavity growth and sinkhole collapse in Dead Sea materials in PFC2D v5.0

B.5.1 A PFC and Python based code to simulate sinkhole formation

A graphical description of the implemented Python/PFC2D-fish sinkhole modelling code is depicted in Figure 24. Here, fish code parts are marked in yellowish, Python code in greyish colour. A typical sinkhole simulation follows the scheme:

1. Model dimensions, particle parameters and a function $f(i)$ for the material removal is defined at the beginning of each set. An unbonded assembly of particles with a fixed porosity of 0.2 is generated at once for the whole assembly at the initial void space growth round ($i = 0$, no material removal yet).

2. Similar to the material generation procedure for the model verification material (cf. A.2), we settle and bond the assembly with a PBM according to the desired material properties. It has to be noted that for low-strength material a bond-reinstallation procedure has been applied, a so called annealing, i.e. failed bonds can be re-established by contact with other particles of the same material, accounting for e.g. cohesive mud behaviour. For the other materials a failed PB is not activated again. We then install the desired tracking functions (measurement circles, marker particles, histories) and group the initial void spaces defined in the model control file.

3. This material removal loop acts on each defined cavity growth round i. If the area of the particles in the void space zones matches the definition by function $f(i)$, the loop is broken and important tracked parameters are recorded.

4. Step 3 is repeating with increasing material removal round i, and after each, the desired tracked results are output via Python code. When a pre-defined maximum void space growth is reached, the model is finished and a new random assembly starts at step 1.
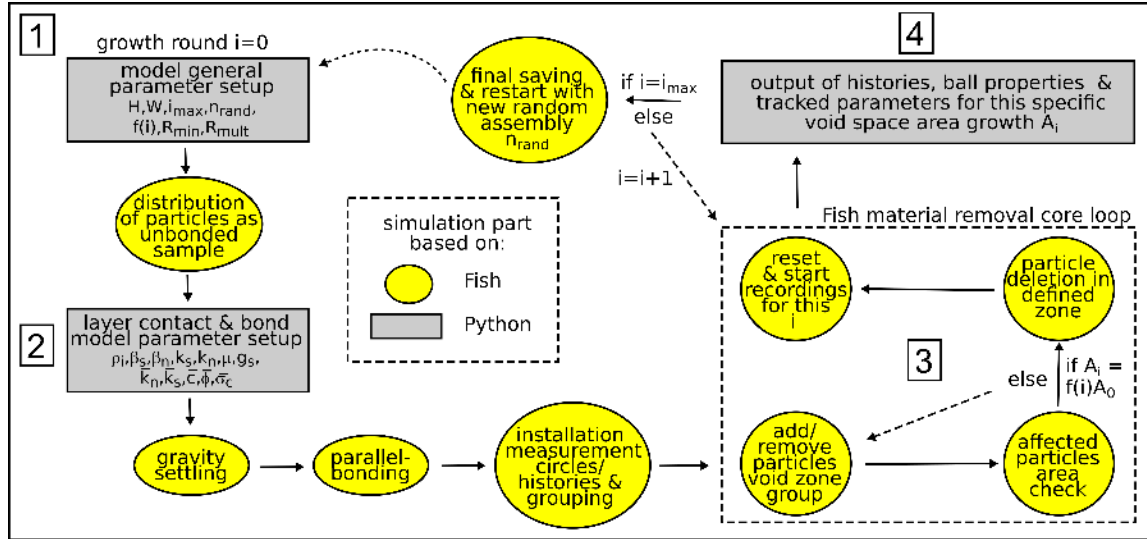
Figure 24: Graphical Description of the PFC2D based sinkhole modelling code. Yellow colours indicate PFC-fish language based code, grey colours are Python control connections. Solid arrows indicate timestep cycling. Each model set consists of n_{rand} random assemblies of particles to account for statistical variation of the DEM Sinkhole collapse via arbitrary material removal function in single voids

To avoid another degree of freedom in the calibration of micro- vs. macroproperties, the initial porosity only changes due to the compression by the gravity settling scheme. We have refrained from using either post-settling particle removal to adjust the porosities to specific values or layer-wise gravity deposition with different porosities because of the high amount of calculation time needed.

The fish material removal core loop (No. 3 in Figure 24) provides the technical implementation of a quasi-static void space growth. A simple law between the particle area A_i that is supposed to be removed during the void space growth round i and the initial area A_0 has been chosen with arbitrarily definable function $f(i)$:

$$A_i = f(i,..)A_0 \qquad\qquad (\ 12\ )$$

The void space area is defined by a major and minor axis. This enables both semi elliptical, elliptical and circular void space growth. For the results presented in this manuscript, a slow, constant void space growth $f(i) = 1.0^i$ with $A_0 = 16.3$ m^2 and a linear eccentricity of $e = 2.64$ was chosen. This avoids the triggering of dynamic effects if too many particles are deleted at once. Other options may include a doubling void space each round ($f(i) = 2.0^{i-1}$ or an exponential increase $f(i) = e^{(i-1)}$ for $i \geq 1$. For this purpose, a computationally rather cost intensive static equilibrium procedure is available in PFC2D v5, which sets the bond strengths high before particle deletion, cycles to a stable limit after particle deletion and then resets the bond strengths to the original value.

The pure runtime for a full simulation of an alluvium on mud setup on an Xeon 3.7 Ghz processor with 64 GB RAM needs roughly 2 weeks for one particle assembly without tracking geophysical parameters. The tracking would increase the runtime by a factor of ~1.5. A possible improvement in future will be the introduction of focus regions with an increasing particle radius with distance from the centre of the model.

B.5.2 Details on the implemented parameter tracking

A tracking of pre-, syn- and post-collapse geodetic and geophysical parameters has been implemented in the modelling code (No. 4 in Figure 24). The technical details are listed as follows.

Porosity, stress and strain rate are recorded using the distribution of so-called measurement circles of area A^m throughout the model domain (Itasca Cooperation Group, 2014; Potyondy and Cundall, 2004).

Porosity is calculated via: $n = \frac{V_{void}}{V_m} = 1 - \frac{V_{mat}}{V_m}$ with V_{void} as the volume of the void and V_{mat} the approximated volume of the particles of amount N_b in the measurement circle.

The average **stress** tensor is calculated in static conditions via: $\bar{\sigma} = -\frac{1}{V_m}\sum_{N_c} F^{(c)} \times L^{(c)}$ where $\times$ is the dyadic product of two tensors, N_c is the number of contacts, $F^{(c)}$ is the contact force vector and $L^{(c)}$ the branch vector that joins the centroids of two entities. From this, the maximum compression principal stress σ_1, the minimum compression principal stress σ_3 and the maximum shear stress $T_{max} = \frac{(\sigma_3 - \sigma_1)}{2}$ is calculated, which is always positive in the convention used here, where compression is negative.

The **strain rate** tensor $\dot{e}$ (velocity gradient tensor) is calculated via a least-squares best fit approach of the predicted vs. the measured relative velocities $\tilde{V}_i^{(p)} = V_i^{(p)} - \bar{V}_i$ between each two entities p during a timestep i, with $V_i^{(p)}$ as the translational velocity and $\bar{V}_i = \frac{\Sigma_{N_p} V_i^{(p)}}{N_p}$ as the mean velocity in the circle area.

5 The **strain** tensor in the measurement region is then calculated by multiplying strain rate components with the simulation time-step and summing over the desired period.

Alternatively, **strain** is calculated via simulated extensometers. For these pairs of particles are defined which lie either horizontally or vertically next to each other. By registering the displacement of each particle, a pairwise calculation of the 10 horizontal and vertical strain is achieved at low computational cost in comparison to the measurement circle distribution (Itasca Cooperation Group, 2014).